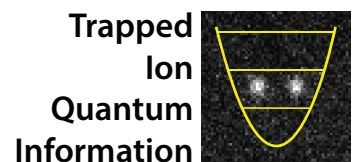




Eidgenössische Technische Hochschule Zürich
Swiss Federal Institute of Technology Zurich



ETH Zürich, Department of Physics

MASTER THESIS

CRYOGENIC SETUP FOR
FAST MANIPULATION OF THE QUANTUM
MOTIONAL STATES OF TRAPPED IONS

Supervisor:
Prof. Dr. Jonathan Home

Student:
Matteo Fadel

Spring Semester 2013

Contents

Introduction	2
1 Quantum Motional States of Trapped Ions and their Manipulation	4
1.1 Ion Trapping	4
1.2 Quantum States	5
1.3 Fast Control of Motional States	5
1.4 Proposed Experiments	5
1.4.1 Fast ion transport	6
1.4.2 Motional state squeezing	7
1.4.3 Other experiments	8
2 Experimental Setup	9
3 Cryorefrigerator	12
3.1 Pulse Tube Cooling	12
3.1.1 The CRYOMECH PT410	13
3.2 Helium Liquifier (recondenser)	14
3.2.1 Temperature Sensors	14
3.2.2 Heat Load	14
4 RF Resonator	16
4.1 Requirements	16
4.2 Design	16
4.3 Performance	17
5 Fast Switching Electronics	22
5.1 Requirements	22
5.2 Overview	22
5.3 Cryo-Electronics Board	23
5.3.1 Passive electronics	23
5.3.2 Switches	24
5.4 Feedthroughs and cabling	25
5.5 Pulse Generation and Digital Control Electronics	25
5.6 Characterization	28
5.6.1 Measurements description	28
6 Summary	38
References	38

Introduction

Among the many possible applications, ion trapping is nowadays largely used for high-precision spectroscopy, accurate time measurement, quantum electrodynamics tests or quantum computation [1–3]. In this context, trapping means confining one or more charged particles in a small region by means of electric and magnetic fields. An interesting case is that of single valence-electron atoms, such as alkaline-earth metals singly ionized (e.g. ${}^9\text{Be}^+$, ${}^{40}\text{Ca}^+$), because they can be characterized by an internal quantum state, the electronic energy level, and an external quantum state, associated to their motion inside the trapping potential.

The internal electronic state can make up a qubit system so long as long-lived states (such as the ground state and a dipole forbidden or a hyperfine level) are chosen. In order to perform quantum logic operations, i.e. gates with more than one qubit, multiple ions can be trapped and crystallized into a chain, with the common modes of motion serving as a quantum bus [4]. The controlled manipulation of the ions' motion can also be used to transmit quantum information between different regions of a trap array [5,6]. Furthermore, manipulating the harmonic oscillator motional states has also led to more fundamental results such as the preparation of non-classical states of motion (examples include Fock states, coherent states, squeezed states, superpositions of states, entangled states, Schrödinger-cat states) [7–12].

Motional states can be controlled by the application of electromagnetic fields (laser, microwave), or by changing the trapping potential. The latter allows for fast and large changes in the motion of the ion, independent of the ions' internal state. It can be realized by generating time-varying potentials outside the vacuum system, using DACs or voltage suppliers, and connecting them to the trap electrodes via feedthroughs. The main limitation of this setup is given by capacitances present in the lines going to the electrodes, which in the best case allow to vary the potentials over a time corresponding to few oscillation cycles of the ion [13, 14].

Manipulation of the motional states of a trapped ion in timescales faster than its oscillation frequency would open up new possibilities. In quantum information processing, for example, a fast way to transport informations between different regions of the processor is of primary importance in order to scale to large number of ions. A number of experiments already demonstrated the feasibility of ion transport through array of traps by variations in the trapping potentials slower than the oscillation frequency of the ion(s), showing the need of a compromise between the operation (transport) time and the amount of motional excitation which persists after the transport has taken place (which should be minimized since errors in multi-qubit quantum logic gates increase for higher motional excitation) [13–19]. More recently, our group proposed that a new scheme for supplying voltages to trap electrodes would allow changes to the trapping potential on timescales 100 times shorter than the period of the oscillation frequency of the ion, resulting in a new transport regime faster than a single cycle of oscillation in the trap [20].

This thesis presents the experimental setup for implementing this novel method to supply fast voltages to trap electrodes, which involves placing electronic switches inside the vacuum system and in a cryogenic environment. By controlling the switches with digital signals, they allow trap electrodes to be switched between input potentials supplied by analog supplies, on timescales much faster than the typical period of oscillation of the ion.

Section 1 describes briefly the physics of quantum motional states of trapped ions, together with the fast control scheme proposed to manipulate them, and a description of possible experiments that can be done. Section 2 presents an overview of the experimental setup needed to implement the proposed experiments. The parts of this setup described in detail in this thesis are: the cryo-refrigerator in section 3, the RF resonator in

Introduction

section 4, and the fast electronics in section 5. Conclusions, further possible improvements and applications can be found in section 6.

1 Quantum Motional States of Trapped Ions and their Manipulation

1.1 Ion Trapping

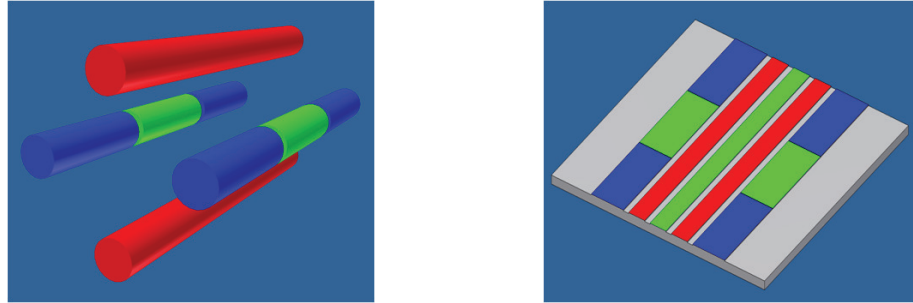


Figure 1: Linear Paul trap (left) and planar Paul trap (right). RF electrodes are shown in red, control electrodes (RF ground) in blue and green.

After a free atom has been produced, and ionized with lasers, a potential minimum is required to trap it. Since static electric fields cannot provide a 3D minimum, a possible solution to confine the charged particle is to use RF and DC voltages applied to a specific geometry of electrodes, in a configuration known as a Paul trap, figure 1 (left).

A more recent development is with electrodes placed in the same plane, as in the planar Paul trap in figure 1 (right), [21]. This geometry can be advantageous in the sense that fabrication can make use of precise photolithography processes, alignment is easier and more accurate, and the size can be scaled down. It is also possible to add many other control (RF-grounded) electrodes, that can be used to change the shape of the potential and determine the position of the minimum.

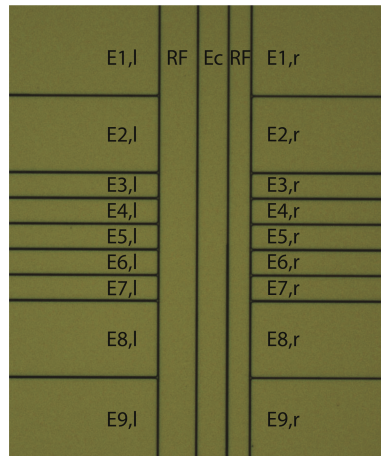


Figure 2: A 500 μm width detail of the planar trap used in the setup.

For the setup proposed in this thesis, the trap shown in figure 2 will be used. It is a planar Paul trap built using photolithography on a quartz wafer. The size of the trap die is 1 cm \times 1 cm, with pads for wire-bonds on the edges. There are 19 control electrodes (Ec, E2l/r and E8l/r are five electrodes which can be supplied with fast-varying potentials), two RF electrodes connected to the same signal, and a cover mesh electrode (not

visible in figure 2).

1.2 Quantum States

The quantum energy eigenstates ψ of a trapped ion described by the Hamiltonian H are solutions of the time independent Schrödinger equation $H\psi = E\psi$, where E is the energy associated to the state. For the case of a hydrogen-like trapped ion, the Hamiltonian itself can be written as the sum of two decoupled terms: one due to the motion of the ion inside the harmonic potential and the second dependent on the orbital occupied by the valence electron.

If the 3D trapping potential is symmetric around the trapping axis, the motional term can be further split in three decoupled contributions: one axial (along the trap axis) component and two radial components.

In the approximation where the ion is a 1-dimensional harmonic oscillator, oscillating in the z (axial) direction, with the energy of an oscillation quantum (phonon) $\hbar\omega_z$, and the valence electron can occupy only the states $|0\rangle$ and $|1\rangle$, with $|E_0 - E_1| = \hbar\omega_{01}$, it is possible to write the Hamiltonian as:

$$H = \hbar\omega_z a^\dagger a + \frac{\hbar}{2}\omega_{01}\sigma, \quad (1)$$

where $\sigma = |1\rangle\langle 1| - |0\rangle\langle 0|$.

The eigenstates are then $|n, q\rangle = |n\rangle|q\rangle$, where $|n\rangle$ is the motional state and $|q\rangle$ the internal (qubit) state of the ion.

1.3 Fast Control of Motional States

For a trapped ion, the motional states can be manipulated by using optical field gradients, or by changing the electric fields which generate the trap itself. While optical fields couple to the internal (electronic) state of the ion, and can therefore in general produce only small variations in its external degrees of freedom, by changing the trap electric fields it is possible to produce large changes in the state of the motion.

The common approach to manipulate trap electric fields is to generate time-varying potentials outside the vacuum system, using DACs or voltage suppliers, and connect them to the trap via feedthroughs (figure 3(b)) The main limit of this setup is that the frequency at which the potentials can be changed is limited by capacitances present in the lines going to the electrodes, therefore in the best case this allows to vary the potentials over a time corresponding to few oscillation cycles of the ion [13, 14].

However, manipulation of motional states faster than the oscillation frequency of the trapped ion could be interesting, and would allow to perform new experiments. In order to access this new regime, a different scheme has been proposed [20], where the key idea is to place electronic switches inside the vacuum system and near the trap, controlled by digital signals from outside (figure 3(c)). This should allow the trap electrodes to be switched between three potential levels spanning $\approx 10V$ (supplied by analog supplies) on nanosecond timescales, 100 times shorter than the period of oscillation of the ion, which is in general between 200 ns and 1 μs [22].

1.4 Proposed Experiments

Described below are some possible experiments that could be performed by means of fast voltage switching.

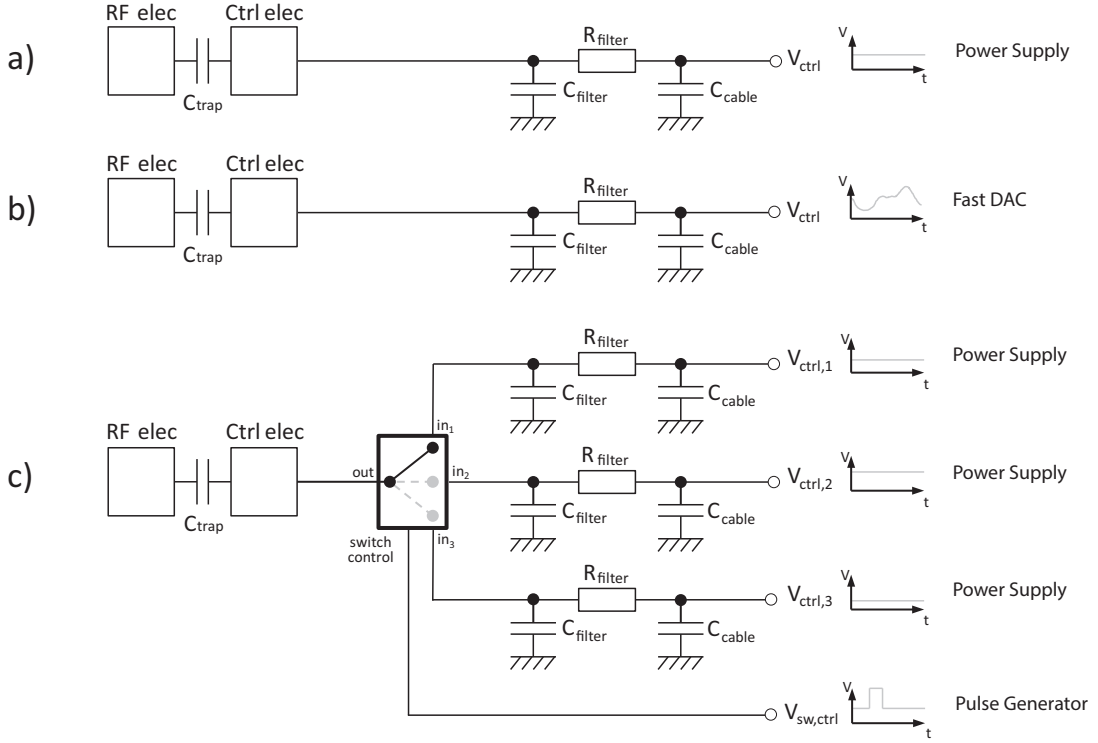


Figure 3: Scheme for supplying potentials at trap control electrodes. (a) constant DC voltage supplied. (b) supply of a time-varying potential with a DAC. (c) the proposed scheme for supply fast time-varying potential using switches near the electrode.

1.4.1 Fast ion transport

Considering the trapped ion as a 1-dimensional harmonic oscillator, a possible routine for fast transport using instantaneous switching of potentials is shown in figure 4.

At time $t < 0$ (figure 4(a)) the ion starts in the ground state of an initial (harmonic) potential well situated at $z = -z_0$, and given by

$$V_{\text{in}}(z) = \frac{1}{2}m\omega_z^2(z + z_0)^2 , \quad (2)$$

where m is the ion's mass. States with minimal minimal uncertainty (i.e. for which $(\Delta x)(\Delta p) = \hbar/2$, like the ground state of an harmonic oscillator) are called coherent states, and in general they can be written as

$$|\alpha\rangle = e^{-\frac{|\alpha|^2}{2}} \sum_n \frac{|\alpha|^2}{\sqrt{n!}} |n\rangle , \quad (3)$$

where α is a dimensionless parameter that corresponds to the “size” of the state as $\alpha = -z_0/a_0$, with $a_0 = \sqrt{\hbar/(2m\omega_z)}$, ($\alpha = 0$ gives the ground state $|0\rangle$).

At $t = 0$ (figure 4(b)) the potential is suddenly displaced to the transport well, which has the same curvature but is centered at $z = 0$. At this point the ion is in a coherent state of the transport well, and under free evolution such a state will evolve into another coherent state. The momentum of the ion will be a periodic function whose mean is zero for $t = n\pi/\omega_z$, with $n \in \mathbb{N}$, corresponding to a rest position. If at $t = \pi/\omega_z$, with the ion being at rest at $z = z_0$, the potential is suddenly displaced again to a final potential well which is centred at $z = z_0$,

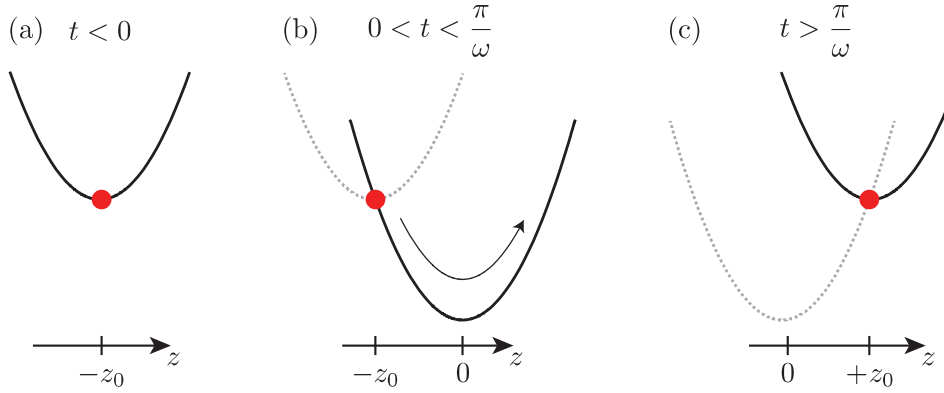


Figure 4: Sketch of the fast transport routine. The ion starts in the motional ground state of a potential well (a). The potential is “instantaneously” switched and the ion starts its coherent oscillation (b). Half an oscillation later, the ion is caught when it has no mean kinetic energy, by switching again the potential (c).

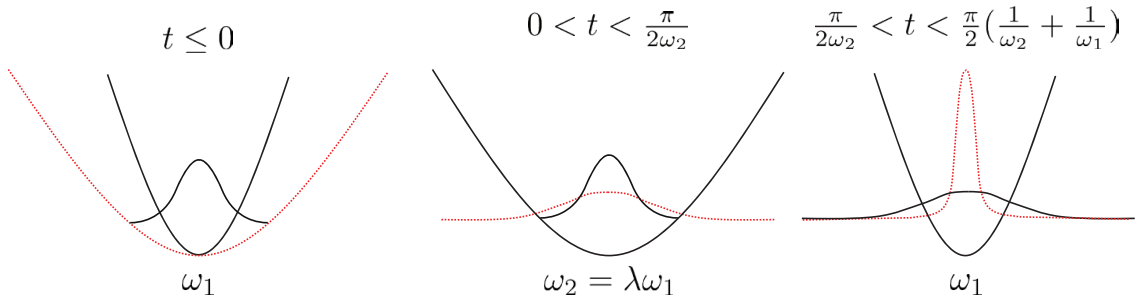


Figure 5: Sketch of the squeezing routine. Black solid lines represent the wave function and the potential at the beginning of the period indicated and red dashed lines at the end of it.

and has the same curvature as the transport well, the ion will end up in the ground state of the final potential, having been transported over a distance of $2z_0$ (figure 4(c)).

A stringent constraint imposed by this routine is the time resolution requirement of $< 20\text{ ps}$ in the switch between the transport and the catch potential, calculated explicitly for a $^{40}\text{Ca}^+$ ion at $\omega_z = 2\pi(1\text{ MHz})$ with $z_0 = 50\text{ }\mu\text{m}$ for an overlap with the ground state of 90% [20]. This imposes a requirement in the stability of the potential to $\approx 10^{-5}$ during the measurement process. Further details and experimental challenges are described in [20].

1.4.2 Motional state squeezing

An alternative application of the fast switching method is in the generation of non-classical states, and one interesting example is vacuum squeezed states.

A coherent state is called squeezed if the quantum fluctuations in one observable are suppressed relative to their value in the ground state (they are increased in the other conjugate observable, satisfying the Heisenberg uncertainty relation) [23].

Fast control of the potential can allow to implement the squeezing procedure proposed in [24]. It involves an abrupt change of the trapping frequency from ω_1 to $\omega_2 = \lambda\omega_1$ at time $t = 0$, followed by the opposite transformation at time $t = \pi/(2\lambda\omega_1)$, as sketched in figure 5. Also here, specific experimental challenges are

reported in [20].

1.4.3 Other experiments

Further applications and experiments that can be implemented are for example the control of the entanglement between radial motional modes of many ions, dynamical studies of a trapped ion, extended transport of ions throughout an array, or interfacing trapped ions and solid-state qubits.

2 Experimental Setup

This section gives an overview of the experimental setup with which trapped ion quantum information experiments are to be performed with surface traps at ETH. It is also the setup in which the switching electronics for fast motional control have been tested and characterized.

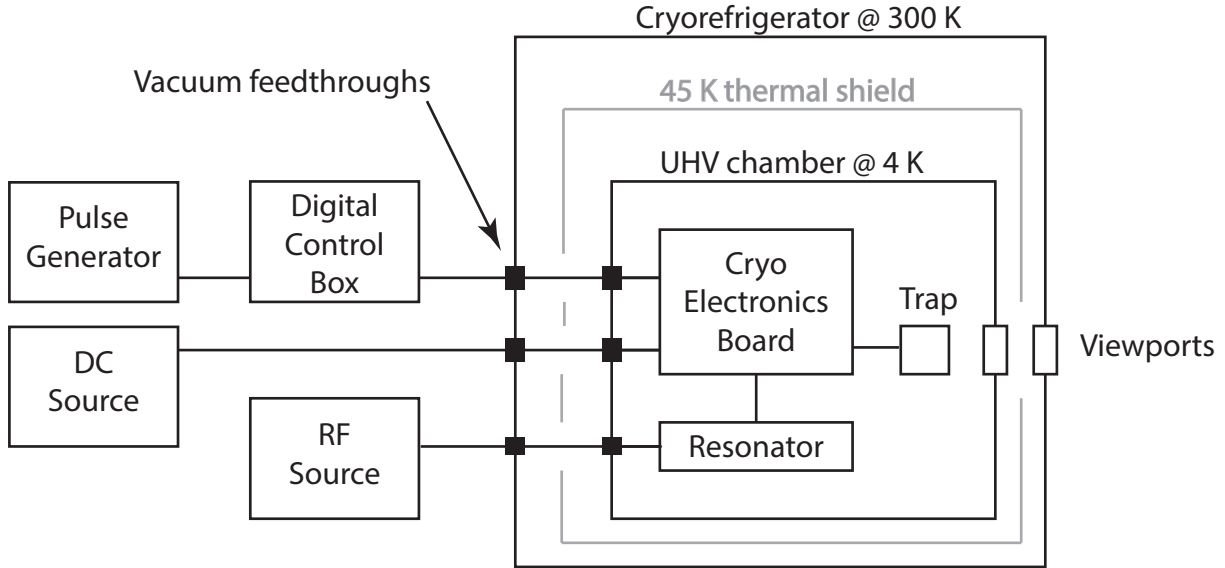


Figure 6: Sketch of the experimental setup.

The experimental setup is sketched in figure 6 (some parts not discussed in this thesis, such as the imaging system, are omitted). The cryorefrigerator keeps the ultra-high vacuum (UHV) chamber at 4 K, in which the trap, the cryo-electronics board (CEB) and the resonator sit. Viewports allow for optical access (for imaging and laser beams) to the trap, whose electrodes are wire-bonded to the CEB. This latter provides fast time-dependent (generated with switches) and DC (filtered) voltages for the control electrodes, and a connection to the resonator for the RF electrode. Vacuum feedthroughs allow for supplying digital control signals and DC voltages for the CEB, and the RF voltage for the resonator from the outside of the cryorefrigerator. Digital control signals are generated by a pulse generator and, if needed, adjusted in time and amplitude by a digital control box, DC and RF voltages come directly from respective sources.

Detailed views of the inside of the cryorefrigerator and of the UHV chamber are shown respectively in figures 7 and 8. A detailed description of the main boxes in figure 6 is presented in the following sections: the cryorefrigerator in section 3, the resonator in section 4 and the fast-switching electronics in section 5.

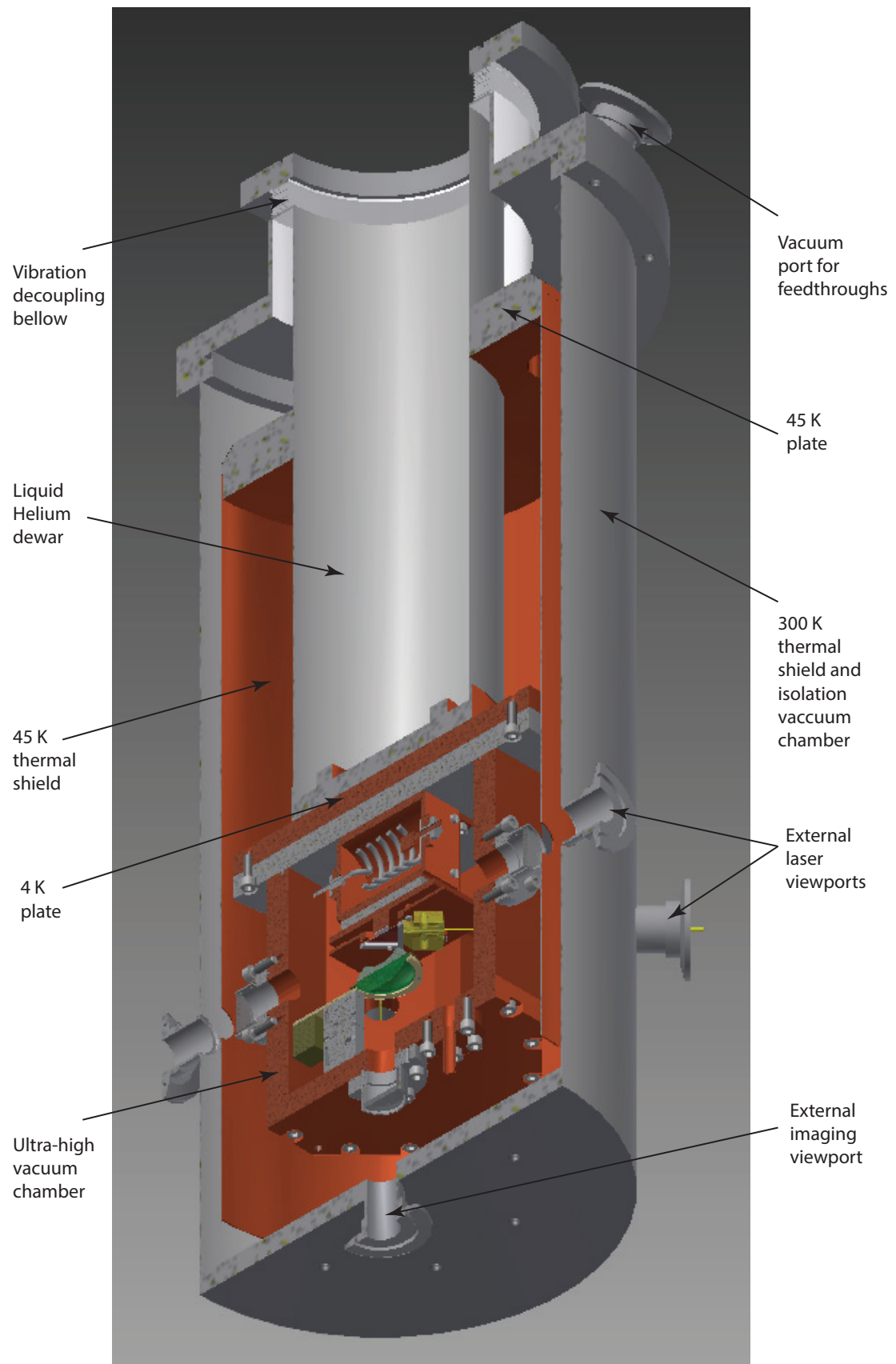


Figure 7: Details of the cryorefrigerator

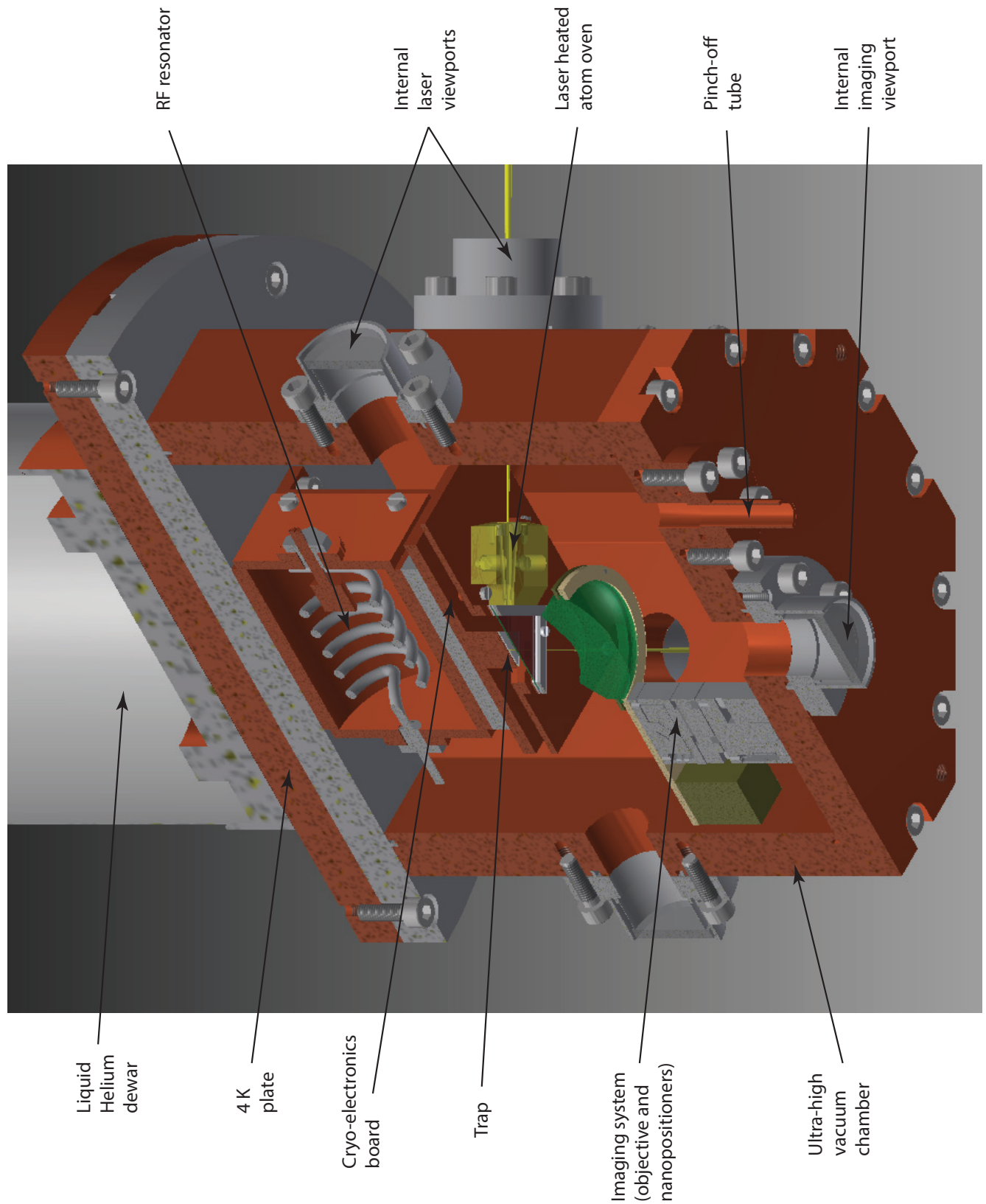


Figure 8: Details of the ultra-high vacuum chamber

3 Cryorefrigerator

A commonly used cryo-cooling device is the pulse tube refrigerator, capable of reaching temperatures of $\approx 2\text{ K}$ using ^4He .

3.1 Pulse Tube Cooling

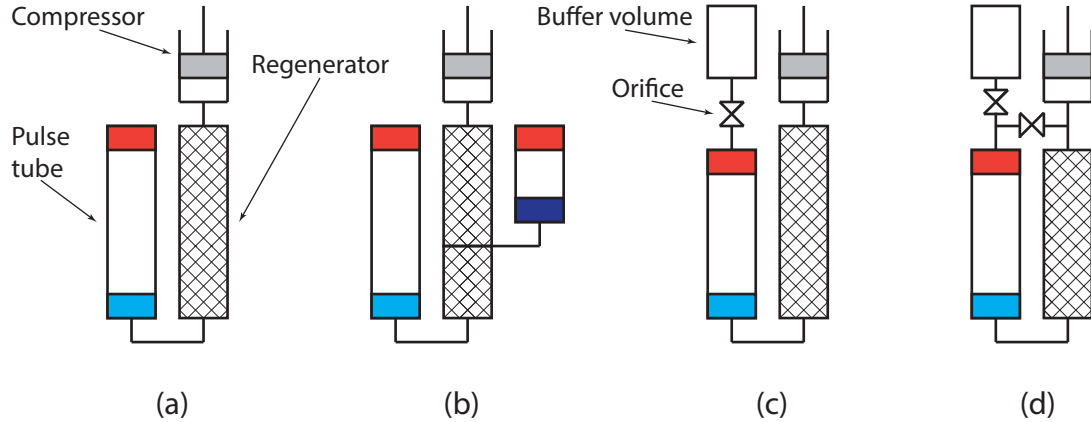


Figure 9: Configurations of different pulse tube cryorefrigerators. Basic pulse tube refrigerator (a), multistage refrigerator (b), orifice refrigerator (c), double inlet refrigerator (d).

Pulse tube coolers are compact, cryogen free, closed-cycle refrigerators. The basic cooler can be built with a compressor, a regenerator and a pulse tube as shown in figure 9 (a), [25].

The compressor, connected to the hot end of the regenerator, creates pressure oscillations of a working gas, which is filling all the system. The regenerator is a tube filled with a porous material having a large heat capacity, and it works as a periodic heat exchanger: in the first half-cycle it absorbs the heat from the gas pumped into the pulse tube (precooling it), and in the second half-cycle it transfers the heat back to the outgoing cold gas. The pulse tube is a tube with two heat-exchanging stages; the hot one is held at room temperature, the cold one is connected to the regenerator.

The cooling cycle can be described as follows. Initially, all the system is filled with gas and at room temperature (figure 10 (A)). During the first half-cycle, the compressor feeds the pulse tube with more gas producing a pressure gradient inside it. This pressure gradient corresponds to a temperature gradient (figure

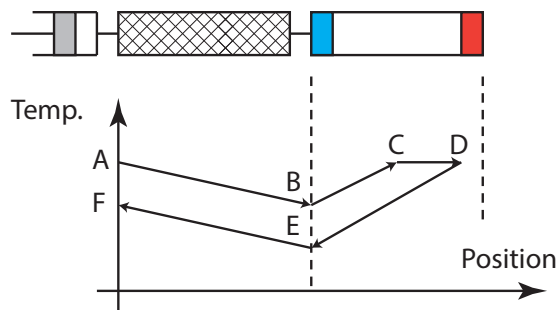


Figure 10: Schematic representation of position and temperature of a gas element inside the pulse tube during a cooling cycle.

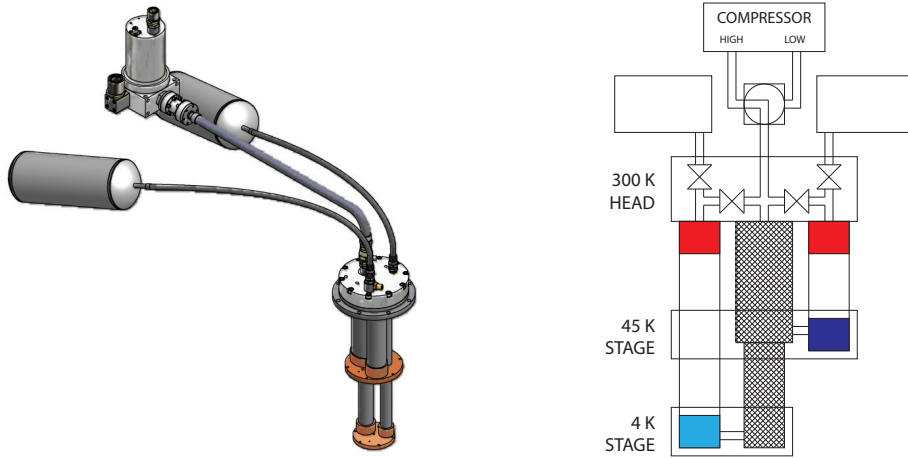


Figure 11: The PT410 pulse tube unit. A 3D drawing (left) [32], and a sketch of the connections between the building components (right) [33]. Note the remote rotary valve, to reduce vibrations at the cold end.

10 (BC)) with a minimum at the cold heat-exchanging stage and a maximum at the hot one, where the hot gas can dissipate its heat (towards the environment) and therefore cool down (figure 10 (CD): temperature remains constant even if pressure increases, due to heat dissipation.). In the second half-cycle, the gas is expanded adiabatically, resulting in a further cooling (figure 10 (DE)) and going back to the compressor the cooled gas absorbs heat from the regenerator, decreasing its temperature (figure 10 (EF)). This latter step allows the next cycle to start with a gas at a lower temperature (figure 10 (F)) since during the successive feedings of the pulse tube (like the one of the first half-cycle) the gas passing through the regenerator gets cooled down (like figure 10 (AB)). This process can continue, ideally, until the working gas starts to liquefy and therefore no longer compressible. But in reality gas properties and thermal exchanges with the environment impose the limit in the lowest temperature achievable.

The working gas usually adopted is helium ${}^4\text{He}$, since with its low boiling point $T_B \approx 4\text{ K}$ at 1 atm (and its monoatomic structure), it performs better than other gasses. This basic pulse tube design can achieve a temperature at the cold head of approximately 120 K, [26].

In order to reach much lower temperatures, one can use multistage refrigerators (figure 9(b)) (where the cold stage of a pulse tube decreases the temperature of the regenerator for the next pulse tube), orifice pulse tube refrigerators (figure 9(c)) (where a valve regulates the flow from the hot end of the pulse tube toward a reservoir), or double inlet pulse tube refrigerators (figure 9(d)) (where the addition of two orifices and a reservoir can establish a phase shift between pressure oscillations and mass flow of the gas within the pulse tube, which increases the cooling efficiency) [27–31].

Combining all these techniques, temperatures as low as 2 K can be achieved, with cooling powers in the order of 1 W at 4.2 K, [32].

3.1.1 The CRYOMECH PT410

The cryorefrigerator chosen for the experiment is the Cryomech PT410, [32]. It is a pulse tube cooler with two stages, as shown in figure 11. The first pulse tube reaches the temperature of 45 K in the cold stage, with a cooling capacity of 35 W, and the second of 4 K, with a cooling capacity of 1 W. With the remote motor option, vibrations due to the rotative valve which creates the pressure waves are well decoupled from the pulse tubes,

and magnetic field fluctuations are reduced.

3.2 Helium Liquifier (recondenser)

The 4K heat-exchanging stage of the PT410 is not connected directly to the experiment but rather used to liquefy and recondense helium gas (${}^4\text{He}$) inside a dewar. The bottom of this dewar is a copper plate which serves as cold head for the experiment (figure 7). In such a way the temperature of the experiment will be more stable than if it were directly connected to the pulse tube, and the decoupling from vibrations is improved by a bellow which holds the pulse tube inside the dewar (figure 7).

3.2.1 Temperature Sensors

Three temperature sensors have been placed to monitor the temperature of the 45K and 4K stages, and inside the UHV chamber. One was mounted, by the manufacturer of the cryorefrigerator, at the 4K head of the pulse tube, inside the dewar. The other two sensors have been placed at the 45K and 4K plates (figure 7).

The sensors chosen are silicon diodes Si410NN, connected to the reading devices M9302 and M9700, all from Scientific Instruments. Since a four-point measurement is performed, resistances introduced by the wires going to the feedthroughs are irrelevant.

3.2.2 Heat Load

Any component of the setup at a temperature higher than that of the cold stages, and in thermal contact with them, will pose a heat load on the cryostat. The heat exchanging mechanisms to consider are heat conductivity and electromagnetic radiation, since convection plays no role inside vacuum setups. Heat loads are mostly due to: 300K (black body) and lasers (during trap operation) radiation coming through viewports, electrical connections between the electronics at 4K and the outside, and the power dissipated by Joule effect in the electronics.

The pulse tube PT410 used can maintain the temperature inside the recondenser below the boiling point of Helium (at $p \approx 1 \text{ atm}$) if the heat load at the 4K stage is below 1W, and therefore, in order not to exceed this load, some precautions in the design were taken. To reduce the heating through radiation, the viewports have to be as small as possible, and the cold stages are covered by reflecting aluminium foil. Furthermore, since the power radiated from a body depends on its temperature as $P \propto T^4$, the introduction of a thermal shield at 45K between the 300K environment and the 4K stage reduces the radiative heat load. To reduce thermal energy exchange with the outside by conduction, the electrical connections have to be made with wires as long and thin as possible, made of a material that has a low thermal conductivity (constantan 2m long wires are used).

Heat-Load Map The heat-load map (figure 12) shows the temperatures of the 45K and 4K plates of the cryostat as a function of the heat load present on them. This plot can be used to estimate the heat load present, as a function of the temperature measured on the two plates.

The test heat loads consist of metal-film resistors fixed on the two cold plates. In the 45K plate two 4.7 Ohm, 2W resistors in series were placed, in order to dissipate a maximum power of 4W. In the 4K plate only one 4.7 Ohm, 2W resistor was placed. Connections with the outside (flange) are made with normal copper wires, whose resistance is negligible. Temperature sensors have been placed on the two cold plates, on the opposite side of the resistors used as test heat loads.

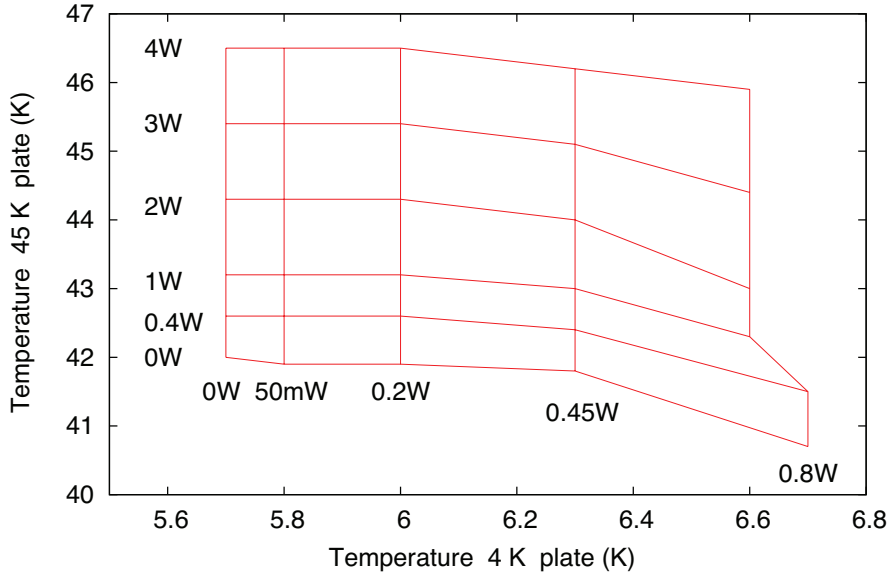


Figure 12: Heat-load map. Temperatures of the 4 K plate and of the 45 K plate are plotted as a function of the heat-load posed on them.

Time	Temperature 4 K plate	Temperature pulse tube	Temperature 45 K plate	Dewar pressure
$t = 0 \text{ s}$	5.7 K	2.6 K	42.5 K	0.20 atm
$t = 5 \text{ s}$	6.3 K	3.5 K	42.4 K	0.44 atm

Table 1: Temperatures at different stages, and pressure inside the helium dewar, for a sudden heat load.

Figure 12 shows a temperature of 5.7 K at the 4 K plate, with zero power dissipated by the test heat loads. This is due to other heat loads present, such as electrical connections (102 constantan wires plus 2 copper wires) and 300 K radiation coming through holes in the 45 K thermal shield. For the same reason, the maximum power that has been possible to dissipate before starting to evaporate helium inside the dewar, was 0.8 W instead of the 1 W expected.

Sudden Heat Load In the proposed setup, ions that are going to be trapped are produced from an atom oven heated with a laser pulse. To test the effect in the temperature of this temporary heat load, a sudden artificial load of 1.8 W (the maximum allowed by the resistor) was dissipated at the 4 K plate.

Figure 1 shows the temperatures at different stages at time $t = 0$ and after 5 s. The temperature at the 4 K plate increases by 10%, and an increase of the pressure inside the dewar can also be seen. (Note that, during ion loading, it could be necessary to heat the oven for a time of $\approx 1 \text{ min}$, but the power dissipated will be $< 1 \text{ W}$.) To avoid big changes in pressure, a stabilization system will be required (a protection valve releases helium when the pressure inside the dewar is above 1.4 atm).

4 RF Resonator

4.1 Requirements

As described in section 1.1, the trap used to perform the proposed experiments is a planar Paul microtrap, which makes use of RF voltage to confine radially the ion. The frequency and the amplitude of this RF signal are key parameters in order to have a stable trapping, and the requested radial motional frequency of the trapped ion.

For proper control of quantum motional states, which requires spectral separation between their energy levels ($\hbar\omega_Z$), the axial frequency of the heaviest ion species that will be trapped ($^{40}\text{Ca}^+$) is chosen to be close to 1 MHz. For the other ion species ($^9\text{Be}^+$), $\omega_Z(\text{Be}) \approx 2\pi(2.1 \text{ MHz})$, since ω_Z goes with the square root of the mass.

Some experiments require trapping more than one ion. In that case, in order to have a crystallized ion chain structure along the trap axis, the radial frequency is typically chosen to be at least four times larger than the axial frequency. By choosing $\omega_{\text{rad}}(\text{Ca}) = 4\omega_Z(\text{Ca})$, one obtains the constraints $\omega_{\text{rad}}(\text{Ca}) = 2\pi(4 \text{ MHz})$ and $\omega_{\text{rad}}(\text{Be}) \approx 2\pi(18 \text{ MHz})$, since ω_{rad} is proportional to the mass.

For an RF voltage $V_{\text{RF}}(t) = V_0 \cos(\Omega_{\text{RF}} t)$, the stability of the ion's motion is determined by the stability parameter q , which must satisfy $q^2 \ll 1$. If this is the case, then

$$\Omega_{\text{RF}} \approx \frac{3\omega_{\text{rad}}}{q}. \quad (4)$$

Inserting in equation (4) the highest radial oscillation frequency, and setting $q = 1/3$, it is possible to find the frequency needed for the RF voltage

$$f_{\text{R}} = \frac{\Omega_{\text{RF}}}{2\pi} \approx 9\omega_{\text{rad}}(\text{Be}) \approx 170 \text{ MHz}. \quad (5)$$

In order to find the amplitude V_0 , one can use

$$\omega_{\text{rad}} \propto \frac{V_0}{m\Omega_{\text{RF}}}, \quad (6)$$

which yields $V_0 \approx 110 \text{ V}$.

Due to the long distance between the trap and the outside of the cryorefrigerator, it is convenient to generate this high-voltage, high-frequency RF signal as close as possible to the trap electrodes. This imposes other constraints, like vacuum and cryo compatibility, compact size and low dissipated power. Furthermore, the frequency at the RF electrode must be as stable as possible throughout the trapping time, in order not to change the pseudo-potential in which the ion sits and therefore its motional state. In other words, the frequency bandwidth Δf_{R} of the RF drive needs to be small, so the quality factor $Q = f_{\text{R}}/\Delta f_{\text{R}}$ shall be large.

4.2 Design

A common solution which satisfies all the requirements above is to use a resonator, placed as close as possible to the trap. Among the different resonator designs, a helical resonator has been chosen (figure 13). The resonance frequency is given by its geometrical dimensions, the Q -value can be of the order of 1000 at low temperatures, and it can be made (except for some insulating parts) of oxygen-free-high-conductivity (OFHC) copper, which is compatible with vacuum and cryogenic environments [34, 35].

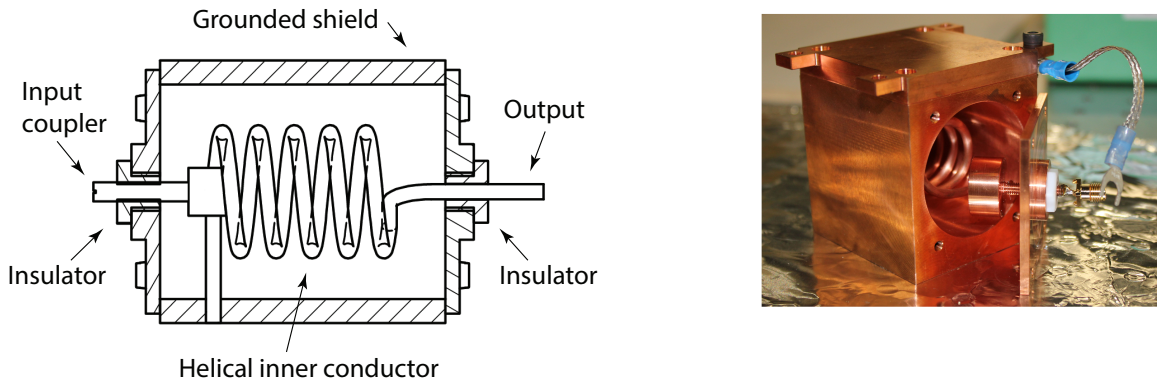


Figure 13: The RF resonator: section (left) and photo (right). The helical coil, shield and input coupler are made out of OFHC copper, while the insulating parts are PTFE.

The resonator built has a tunable input coupler, to match its impedance to the one of the RF generator used as supplier, maximizing the power transfer between the two. The output of the resonator is connected to a pad in the cryo-electronics board, where a track drives the RF signal through wire-bonds to the trap RF electrode (figure 2).

4.3 Performance

The performance of the RF resonator is determined by its resonance frequency and Q -value at 4 K. Variations in the impedance of the resonator, due to cool down and presence of a load at the output, have also been studied.

The resonator is attached to the 4 K copper plate of the cryorefrigerator (figure 7) and the input connected to the 300 K SMA feedthrough via a cryo-compatible coaxial cable (GVLZ034 from GVL). All measurements have been made by connecting a network analyser (Agilent FIELDFOX N9912A) to this feedthrough, adopting the procedures described below.

Impedance matching When the output impedance of the RF source ($50\ \Omega$) is equal to the input impedance of the resonator, a maximum transfer of power is achieved, whereas reflections occur if the two impedances are not matched, which results in lower performance and risk of damaging the source.

With a network analyser, it is possible to find the best matching condition by tuning the input coupler of the resonator (figure 13) until the amplitude of the resonance dip (figure 14, top) is maximized. In the plot, the vertical scale of the instrument corresponds to the ratio between reflected and input power, which should be as small as possible (zero in the ideal matching condition).

Different positions of the coupler cause variations up to 40 dB in the amplitude of the dip (in the unloaded case), and up to 10 MHz in its frequency. In order to fine-tune the impedance seen by the RF source, a matching network with a varactor diode (MA-COM MA46H204) was connected to the input of the resonator (figure 15). By varying the “control voltage” between 1 V and 10 V it is possible to change the capacitance of the diode between 1 pF and 10 pF, and therefore to change the impedance added in parallel with the resonator. It has to be noted that by tuning the capacitance of the varactor diode it is possible to minimize the power reflected by the resonator that would go back to the source (by dissipating it in the diode), and not to change the power transmitted into the resonator (as can be done by moving the input coupler). An advantage of this

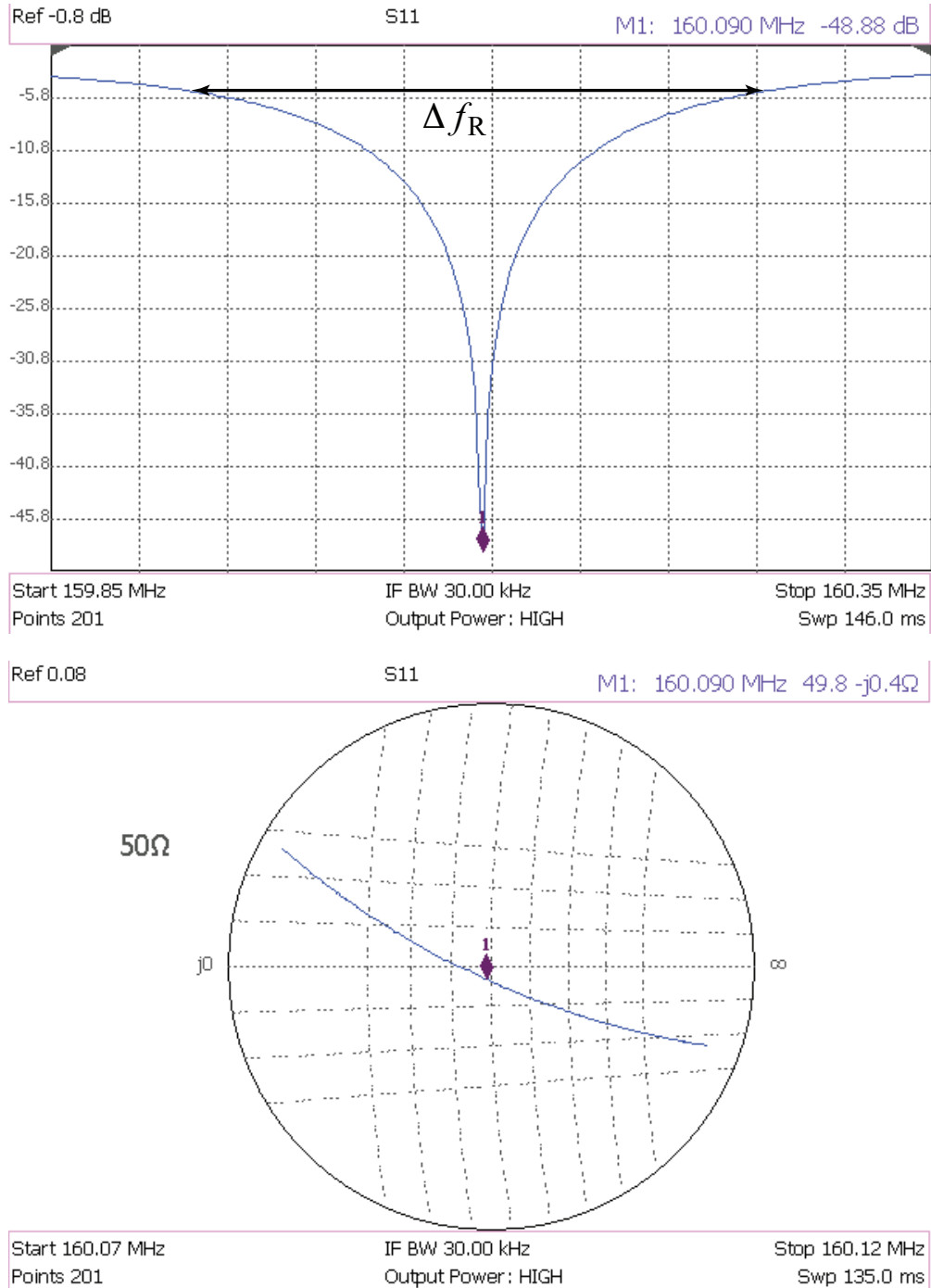


Figure 14: (Top) Reflected power as a function of the input frequency for the case of the unloaded resonator at 300 K, as seen from the network analyser. The marker position shows a resonance frequency of 160.09 MHz, and a ratio between reflected and input power of -48.88 dB . (Bottom) The Smith chart (where the impedance is plotted as a function of the frequency) shows an input impedance very close to 50Ω at the resonance frequency.

matching network is that it works at 4K, allowing to change the impedance seen by the RF source just by varying a DC voltage (and not by moving the input coupler of the resonator, which would be impossible when the cryorefrigerator is working) and has therefore been used to understand how the impedance of the resonator changes at 4K. In any case, the impedance-matching network can be used just for tests, and not during ion trapping when a high power RF signal is required, because the current going through the diode can exceed the maximum allowed by the device.

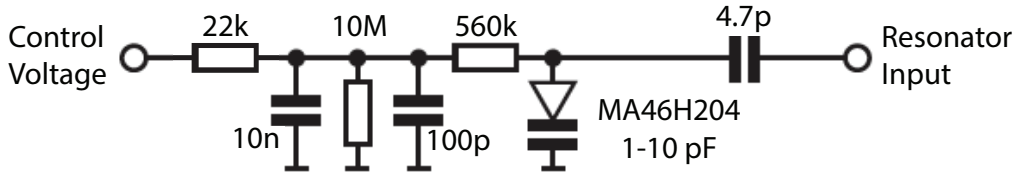


Figure 15: Impedance matching network with varactor diode.

For the unloaded resonator at 300K, the amplitude of the resonance dip can reach values of up to -60 dB, while in the loaded case (described below) the amplitude is ≈ -10 dB. Starting from a “matched” resonator at 300K, the cooling to 4K increases the depth of the dip by ≈ -10 dB (in both the loaded and unloaded cases). By using the impedance-matching network, it is possible to see that the resonance dip corresponding to the (best) matching condition sits at a frequency approximately 150 kHz lower than the one seen without changing the impedance set at 300K. However, the difference in amplitude between these two dips is just of few dB, small with respect to the amplitude of the dip itself. This means that starting from a “matched” resonator at 300K, it is in general not necessary to tune its impedance after the cooling to 4K. All measurements below have been performed with the resonator in the best matching condition at 300K.

Resonance frequency and Q -value f_R is the frequency of the resonance dip. For a given resonator, it depends on the position of the input coupler, on the load and on the temperature.

To measure the Q -value, $Q = f_R/\Delta f_R$, the bandwidth Δf_R is needed, defined as the full width at half maximum of the resonance dip, in power scale. The Q -value itself depends strongly on the temperature, since $Q \propto 1/R_{Cu}$ and copper resistivity is three orders of magnitude less at 4K than at 300K, but less on the position of the input coupler and the load.

The first measurements yielded a surprisingly low Q -value at 4K, as can be seen from table 2. Presumably, this was because measurements were taken after a long (days) exposure of the resonator to air, which oxidizes the copper structure. The oxide layer can be hundreds of nanometres thick, small in comparison to the skin depth at 300K for a 150 MHz signal in copper, which is $\approx 5\text{ }\mu\text{m}$, and therefore a variation in the effective resistance of the oxidized copper is expected to be very small with respect to the pure copper metal. Things change at 4K, where the skin depth drops down to $\approx 200\text{ nm}$, comparable with the oxide layer thickness.

The effect of an oxide layer can be observed by comparing the Q -values for the unloaded resonator, measured before and right after cleaning the resonator with sandpaper until a shiny copper surface was obtained (table 2). At 4K, the Q -value for the cleaned unloaded resonator is three times bigger than before cleaning. It is still not three orders of magnitude bigger than at 300K, as would be expected from $Q \propto 1/R_{Cu}$, probably due to the presence of remnant oxide on the surface.

The significantly negative effects of oxidation force to keep the (surface of the) resonator as clean as possible, and if possible in a vacuum environment, in order to achieve the highest performances.

Temperature	Before cleaning		After cleaning	
	f_R	Q -value	f_R	Q -value
300 K	160.1 MHz	450	162.0 MHz	450
4 K	161.0 MHz	580	162.8 MHz	1800

Table 2: Resonance frequency and Q -value of the unloaded resonator, before and after cleaning from copper oxide.

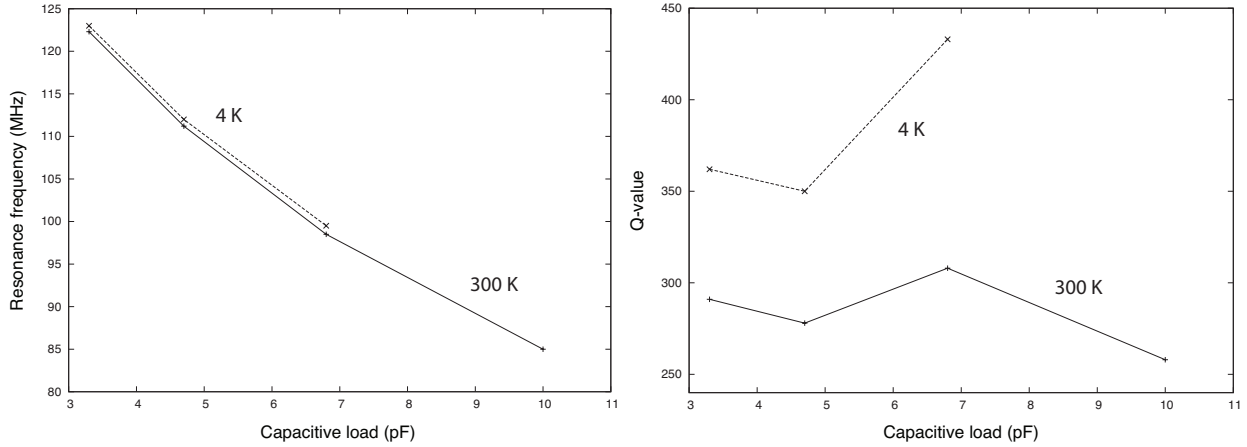


Figure 16: Resonance frequencies (left) and Q -values (right) for different loads at 300 K and 4 K.

Loaded output To simulate the capacitive load of the trap due to the proximity of RF and DC electrodes, different cryo-compatible SMD capacitors (thin-film AVX Accu-P series) have been soldered to the output of the resonator. f_R and Q -value measurements have been repeated under this condition, in order to understand the behaviour of the resonator when the trap is connected, and are reported in figure 16. The resonance frequency decreases with the load (figure 16, left), while the Q -value (figure 16, right) does not have a clear dependence on the load. This can be explained by the fact that the different capacitors used as loads, have different self-resonance frequencies and losses (since a real capacitor has also an inductive and resistive component).

The plot of $1/f_R^2$ as a function of C_{load} (figure 17) shows a clear linear relation between the two, namely that

$$f_R \propto \frac{1}{\sqrt{C_{\text{load}}}} . \quad (7)$$

For the planar trap used in the setup the capacitive load can be expected to be ≈ 3 pF, giving (according to figure 16) $f_R \approx 126$ MHz and $Q \approx 350$. As a consequence, the amplitude of the RF signal going to the trap RF electrode has to be $V_0 \approx 60$ V, to obtain $q = 1/3$ for ${}^9\text{Be}^+$ (see equations (5) and (6)). The next step would be to attach the output of the resonator to a dummy trap, check the results and, if necessary, rebuild the resonator.

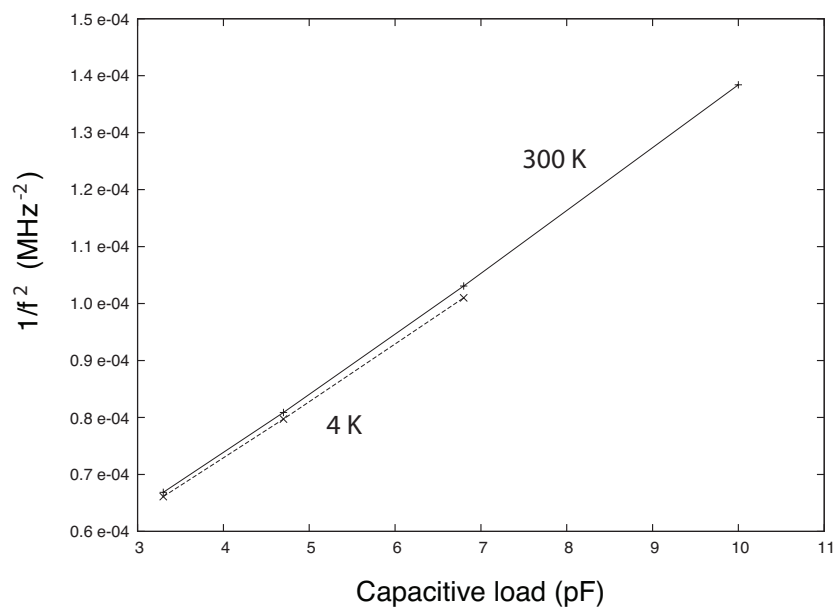


Figure 17: Plot of the inverse of the resonance frequency squared, as a function of the capacitive load at the output, at 300 K and 4 K.

5 Fast Switching Electronics

5.1 Requirements

The proposed fast manipulation of quantum motional states of trapped ions requires a change in the potential much faster than the axial oscillation periods of the ions themselves. If we consider a $^{40}\text{Ca}^+$ ion with period $T_{\text{ax}} \approx 1\text{ }\mu\text{s}$, trapping potential changes must occur by variations (switching) of the voltages at the control electrodes in a time $T_{\text{sw}} < T_{\text{ax}}/100 \approx 10\text{ ns}$. Slower, but still diabatic, changes might introduce more complications like uncontrolled excitation of motional states or even loss of information during qubit transport, due to couplings between motional and electronic states.

A common scheme to supply time-dependent voltages to trap control electrodes is by using DACs or voltage supplies from the outside of the vacuum system containing the trap itself, the main reason for not being in vacuum being release of gases from electronic devices at room temperature, that will end up compromising vacuum quality and therefore the ion's lifetime. Supplying control electrodes over large distances (and through vacuum feedthroughs) can introduce and pick up noise which would need to be filtered. Typically, RC low-pass filters are placed near the trap, to attenuate high-frequency noise components but inevitably reduce the switching speed.

In order to access the required nano-second switching timescale, a possible solution is to control the needed potentials inside the vacuum system by placing fast switches close to trap electrodes, as proposed in [20]. In the setup described in section 2, this means that the switches have to work at 4K.

An additional requirement is the simultaneous switching of potentials at trap electrodes. Since there are asymmetries in the electronics (different switches, different length of wires, ...), the switches must be controlled independently, in order to be able to introduce delays in the control lines, which take into account different propagation times of signals. This implies also that the electronics generating the control signals must be able to introduce delays in the pico-second timescale.

Moreover, to perform the fast transport experiment proposed in section 1, a time accuracy $< 20\text{ ps}$ is needed to catch the ion in the ground state with a 90% likelihood for a transport distance of $100\text{ }\mu\text{m}$.

Other, relevant requirements for the switch are: low power consumption (to minimize the heat load inside the cryorefrigerator), a deterministic voltage drop across the closed switch, the capability to switch potentials which span over $\approx 10\text{ V}$ (to perform the experiments proposed in section 1) and a low noise introduction (to minimize the presence of noise at the electrodes).

5.2 Overview

A conceptual scheme of the circuit needed to generate the fast time-dependent control potentials is given in figure 3 (c). It is realized in the setup shown in figure 6, where the trap electrodes are wire-bonded to the cryo-electronics board (CEB), inside an ultra-high vacuum chamber cooled down to 4K. All electronic signals (digital controls for the switches, DC voltages) are supplied via microD-51 feedthroughs at the 4K stage. 2m long lines connect the vacuum system with another set of feedthroughs at the 300K stage, where voltage supplies and digital control signals generators are connected. A detailed description of these parts is given below.

5.3 Cryo-Electronics Board

The cryo-electronics board (CEB) (figure 18) is the interface between voltage/signal sources and the trap, placed inside the vacuum can at 4K (figure 6). It includes electronics for three different purposes: the switch circuitry for the 5 switchable control electrodes, the RC low-pass filters for the other 15 (non-switchable) control electrodes, and the RF track for the RF electrode.

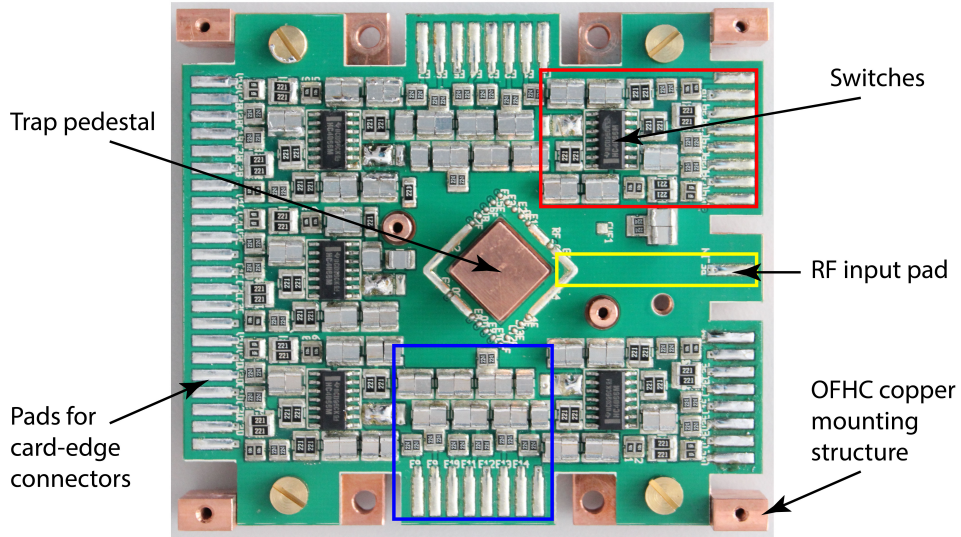


Figure 18: The cryo-electronics board on the copper mounting part. Marked are the circuitry relative to three switches (red), seven RC filters (blue) and the position of the RF track (inside the PCB, yellow). The CEB is mounted on a copper structure for thermal contact to the cold plate.

On the CEB, small pads near the center allow for wire-bonds to the trap electrodes, and pads on the edges allow for five card-edge connectors (Sullins HCXXDREN) which go to the 4K feedthroughs inside the chamber. Special care was taken to minimize the vertical distance to be bridged by the wire-bonds, while keeping the optical access free for the lasers going to the trap.

5.3.1 Passive electronics

To connect the resonator output to the trap RF electrode, a straight track has been routed in the CEB. On both ends of this track there is a pad which allows, on one side, for soldering the output of the resonator and, on the other side, for wire-bonding to the RF electrode.

14 trap electrodes, plus a cover electrode on top of the trap, are supplied by DC voltages. To remove the noise picked up by the long lines connecting 300 K to 4 K feedthroughs, low-pass RC filters have been designed and placed near the trap electrodes. They also ensure the RF-grounding of the control electrodes. The components chosen are $R = 110 \text{ k}\Omega$ (thin-film resistor) and $C = 200 \text{ nF}$ (Panasonic ECHU(X) series, showing an impedance $< 1 \Omega$ at 100 MHz), giving a cutoff frequency $f_c = 1/(2\pi RC) \approx 7 \text{ Hz}$.

5.3.2 Switches

A number of commercial integrated circuit (IC) switches were tested and characterized at 4 K [36]. Among different technologies and products, the device chosen was the CMOS IC CD74HC4066M, from Texas Instruments, which implements four bilateral single-pole-single-throw (SPST) switches [37].

The additional circuitry added to one of these SPSTs, as implemented in the CEB, is shown in figure 19, together with the connection between three SPSTs and the trap control electrode, in order to realize the scheme shown in figure 3.

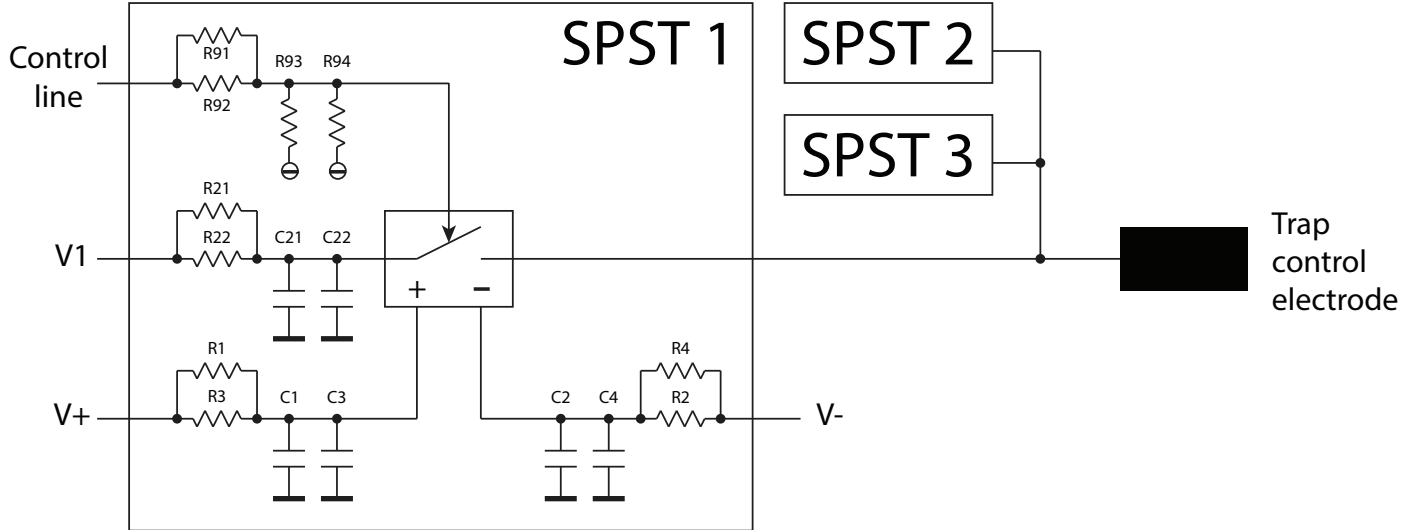


Figure 19: Circuitry relative to one SPST and connection to the trap control electrode.

More explicitly, the components have the following functions:

- R1, R2, R3, R4, C1, C2, C3, C4 form low-pass filters for the power supplies of the SPST (V_+ , V_-), with a cutoff frequency of $f_c \approx 7\text{ kHz}$,
- R21, R22, C21, C22 form low-pass filters for the input DC voltages that go to the electrode ($V_{1,2,3}$), with a cutoff frequency of $f_c \approx 7\text{ Hz}$,
- R91, R92, R93, R94 are the protection and the pull-down resistors for the control lines of the SPST,

Each resistor and capacitor is “doubled” in order to prevent a failure due to the cool-down of the board, which can cause the breaking of solder points.

V_+ and V_- is the power supply of the switch, V_1 is one of the three voltages at which the trap electrode has to be switched, and the “control line” is the digital signal controlling the state (open/closed) of the SPST. According to the IC datasheet, it is required to have: $((V_+) - (V_-)) = 9\text{ V}$, $V_+ \geq V_1 \geq V_-$, and the SPST is open (closed) if the “control line” is at V_- (V_+).

In the CEB there are 5 circuits like the one shown in figure 19, allowing the supply of 5 trap control electrodes with fast time-dependent signals.

5.4 Feedthroughs and cabling

Electrical connections are needed between the outside of the cryorefrigerator and the inside of the vacuum chamber (figure 6).

For the RF signal that goes to the resonator, SMA feedthroughs are used at the 300K stage and at the vacuum chamber at 4K. The connection between them is done with a cryo-compatible coaxial cable (GVLZ034 from GVL).

For the CEB, a large number of lines are needed: 15 fast “control lines” with 15 associated ground-wires (to close the current loop), 15 DC potentials ($5 \times V_{1,2,3}$), 2 common $V \pm$ (to supply the switches), and 15 DC potentials going to the non-switchable trap control electrodes. All these are supplied via four microD-51 feedthroughs, two at 300K and two at the vacuum chamber at 4K. Connections between them are realized with 102, 2 m long cables: ribbons of 12 PTFE-insulated constantan twisted pairs for the “control lines” and their respective ground-wires (Oxford Instrument 59-PAZ0038), and PTFE-insulated constantan wires (Omega Eng. TFCI-003-1000) for the DC voltages. The use of long, thin, constantan cables is convenient to reduce the thermal conduction with the outside, and therefore the heat load. However, metals having a high thermal resistance also have a significant electrical resistance, as can be seen from the measurements performed with the different wires at 300K and (in a gradient from 300K to) 4K (table 3).

Cryorefrigerator	Twisted pair resistance	Constantan wire resistance
Off	125Ω	230Ω
On	117Ω	213Ω

Table 3: Resistance of the different 2m long wires.

5.5 Pulse Generation and Digital Control Electronics

15 digital control signals need to be generated to control the 15 SPST. As mentioned before, an SPST is open (closed) if the “control line” (figure 19) is at $V-$ ($V+$), and therefore the control signal amplitude has to be $((V+) - (V-)) = 9\text{ V}$.

The most demanding experiment that will be performed is the fast ion transport (figure 4), which requires the switching between 3 potentials and for which a time resolution $< 20\text{ ps}$ is desirable. This experiment will be therefore considered for the design of the circuit generating the digital control signals.

To perform a fast ion transport routine (figure 4) the potential at one control electrode has to be similar to the one shown in figure 20 (left). In this case, $V_{1,2,3}$ are the voltages that, at one specific electrode, contribute to generate the three potential wells sketched in figure 4.

The digital control signals needed by the three SPSTs to produce the correct time-dependent voltage at the electrode are the pulses shown in figure 20 (right). Different delays $D_{1,2,3}$ with respect to a “trigger” event are introduced since, for precise timing control and synchronization between the switching at different electrodes, different propagation times of the control signals (due to asymmetries in the circuit) need to be taken into account. The widths $T_{1,2,3}$ of the pulses correspond to the duration of a specific potential well, and are in general independent. In the example shown in figure 20, T_2 is the duration of the transport potential, which has to be $\pi/\omega_Z \approx 500\text{ ns}$, while T_1 and T_3 are the durations of the trapping potentials before and after the transport, that in principle can be infinite (for a single transport). Moreover, since the duration of the transport

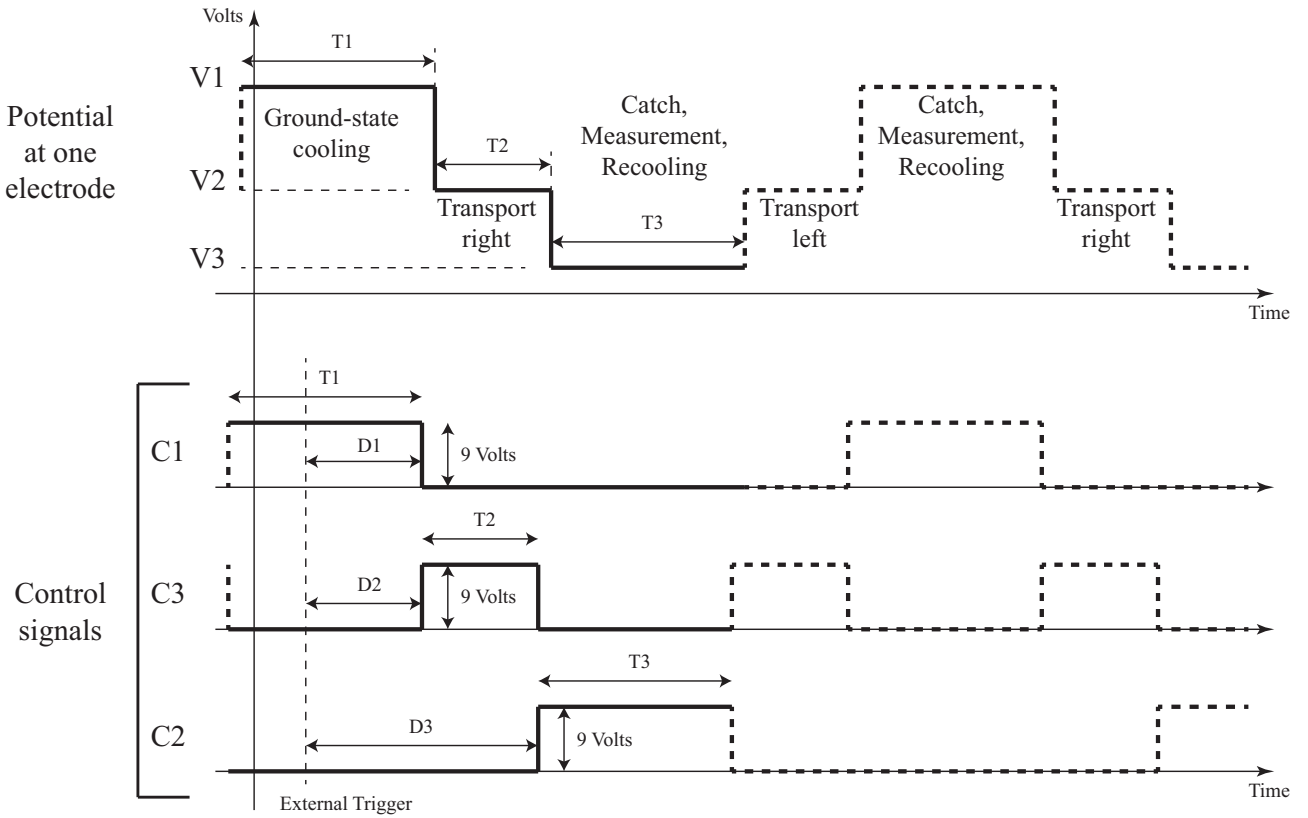


Figure 20: Example of the potential needed at one trap electrode to perform a fast ion transport experiment (left), and control signals used to produce it with 3 SPSTs (right).

potential well is to be performed with a time resolution < 20 ps [20], a time resolution of the same order is needed in the digital control signal.

During an experiment, the switching routine needs to be repeated in order to acquire a significant amount of data, and this can be realized by making digital control signals periodic. To further simplify the generation of these signals, the pulse widths T_1 and T_3 can be set to be equal, and of the order of the time needed to measure and recool the motional state, which in the best case can be ≈ 10 ms. The time accuracy for the switching between different potential wells becomes a requirement in the stability of the control signal period, more precisely the standard deviation of the distribution of periods (jitter, not pulse width) needs to be approximately < 20 ps for the most demanding experiment envisioned in [20].

Digital control signals requirements summary

The requirements for each of the 15 digital control signals are:

- 9 V amplitude, with respect to a reference (biasing) voltage,
- adjustable pulse width, typically 500 ns, with resolution < 100 ps,
- adjustable frequency in the range: DC - 1 MHz,
- adjustable delay with respect to a “trigger” event, with resolution ≈ 20 ps,
- jitter < 20 ps.

Three solutions for the generation of control signals are presented below.

Solution A - Direct The ideal solution consists in finding one (or more) device able to generate by itself the 15 digital control lines satisfying the requirements above, and plugging it directly into the 300 K feedthroughs. The only device tested until this moment is the pulse/pattern generator 12000, from Picosecond [38]. This device satisfies the requirements, but is able to provide just two control signals. The necessity of many devices increases drastically the cost of this solution, making it unsuitable for the final setup. A more economic option is the pulse generator P400 from Highland Technology, which has 4 channels [39] and will be tested soon.

Solution B - Independently amplified control signals Other possible solutions consist in satisfying the requirements listed above by using a number of different devices. An example is given by the digital control setup shown in figure 21. A pulse generator (BNC745 from Berkeley Nucleonics [40]) is used to produce digital control signal, but with an amplitude of ≈ 3 V. These signals need to be amplified by a “Digital Control Box” (DCB) before being driven into the 300 K feedthrough.

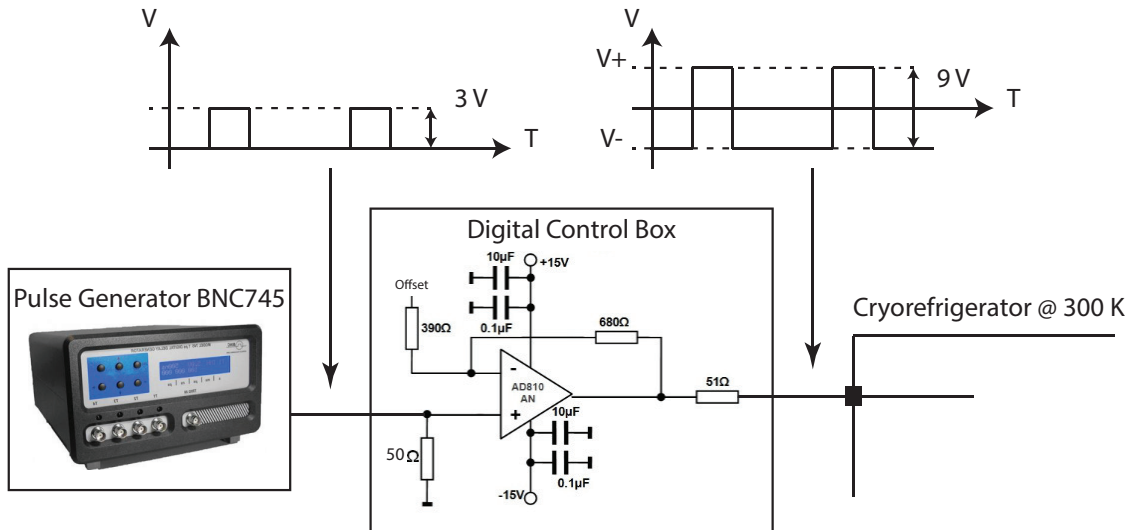


Figure 21: Setup for the generation of digital control signals used for CEB tests.

This setup has been used for a number of measurements, but unfortunately with the BNC745 the pulse width can be changed with 5 ns steps, making it unsuitable for the final setup.

Solution C - Switch matrix and independent delays Since the switching between the three voltages has to occur at the same time at the electrodes, another possible solution consists in the generation of only three independent control signals by a pulse generator, that will be split into 15 signals by a “switch matrix”. 15 independent delays are then introduced at the output of this matrix by specific devices. For this solution, all the electronics devices need to have a low jitter introduction, and delays must be tuned with a resolution of ≈ 100 ps.

5.6 Characterization

5.6.1 Measurements description

Typical measurement setup Figure 22 shows the typical setup used to perform the measurements listed below. The differences between this setup and the final one shown in figure 19 are the presence of the cryo-coaxial cable used to probe the output of the SPST (that will go to the trap electrode), and a “test line” used to probe the input of the SPST bypassing the RC filter.

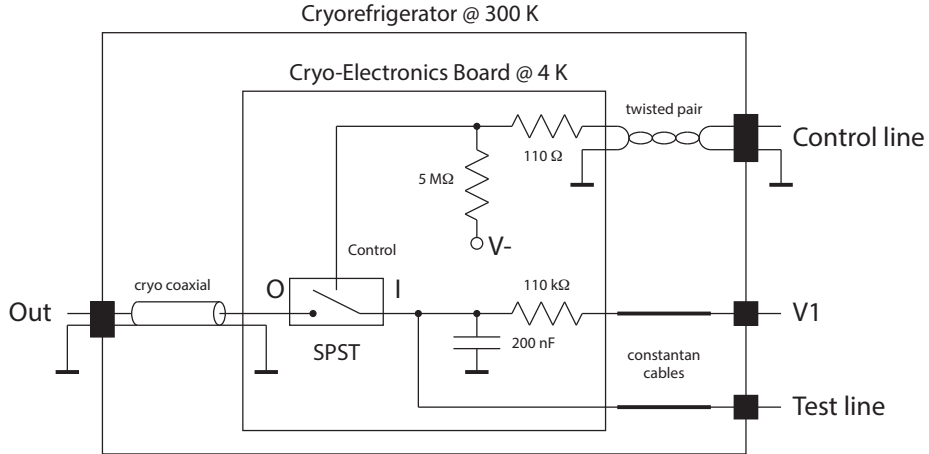


Figure 22: Typical measurement setup.

Any modification to this setup, if needed, will be described in the paragraph relative to the specific measurement considered.

To provide voltages, and perform measurements, different devices have been plugged into the 300 K feedthroughs. Supply of DC potentials, like IC power supply and V1 input voltage, has been provided by TTI power supplies EL302RT. Four-point resistance measurements and DC power consumption have been made with the digital multimeter Keithley 2100. All other measurements have been made with a LeCroy 64MXI-A oscilloscope, which can be used also as a spectrum analyser. Digital control signals have been generated by the function generator SRS DS345, since for the following measurements precise timing is not needed.

Open/Closed resistance For an ideal SPST, the resistance between the input and the output in the open state is expected to be $R_{off} = \infty \Omega$, and in the closed state $R_{on} = 0 \Omega$. A low R_{on} is also important in order to have a proper RF-grounding of the control electrodes (e.g. through the series R_{on} , $C_{21}||C_{22}$ in figure 19).

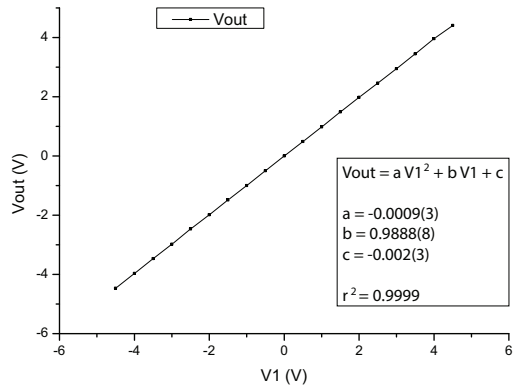
The setup used to measure the resistance across the SPST is the one shown in figure 22, with a modification: two more “test lines” have been connected, one at the input “T” and one at the output “O” of the SPST (figure 22), in order to perform a four-point measurement with the digital multimeter. The main advantage of this procedure is the complete independence of wire resistance in the measurement. Results (table 4) show a low R_{on} at 4K.

Linearity I/O The relation between the voltage at the input and the output of a SPST is required to be linear (preferably of slope equal to 1) for proper experimental control of potential at the trap electrodes.

Temperature	open resistance	closed resistance
300 K	> 10 MΩ	12 Ω
4 K	> 10 MΩ	3.5 Ω

Table 4: Resistance of a SPST open and closed.

This relation has been tested by measuring the output voltage with respect to variation in the input voltage. The setup used is the one shown in figure 22, with a variable voltage source connected at the V1 line, and the digital multimeter at the “out” line. A $V+ = 4.5$ V potential applied at the “control line” holds the SPST closed. Results fitted with a quadratic curve (figure 23) show a good linear relation between SPST input and output at 4 K.

**Figure 23:** Measurements of the output voltage for different input “V1” voltages, at 4 K

Power consumption The power consumption of the IC will have an impact on the heat load on the cryorefrigerator. There are two main contributions: one from the power supply of the IC and the other from the current flowing through digital control lines. The measurement setup is the one shown in figure 22. In the static case (switch held open or closed), currents and voltages have been measured with the digital multimeter, while in the dynamic case (switching at 1 MHz, 50% duty cycle, to study a highly-demanding scenario) they have been measured as RMS values with the oscilloscope (the current has been calculated by measuring the drop across a (100 ± 1) Ω resistor connected in series with the line considered). Results (figure 5) show a negligible power consumption in the static cases, while the dissipated power during continuous switching is 10 mW at 4 K.

Temperature	Open SPST	Closed SPST	1 MHz switching SPST
300 K	< 1 mW	< 1 mW	8 mW
4 K	< 1 mW	< 1 mW	10 mW

Table 5: Power consumption of a SPST open, closed and switching at 1 MHz.

Noise introduction Signals going through closed SPSTs will pick up noise originated from many different phenomena inside the semiconductor, that might end up at the trap electrodes, and can affect the ion motion.

To have a quantitative estimation of the noise introduced by a SPST, it would be possible to compare the power spectra measured before and after the SPST, for example by connecting a spectrum analyser at the “test line” and at the “out” line of the setup shown in figure 22. However, this measurement will be affected by the noise picked up by the long cables, which is much larger than the one introduced by the SPST itself. Therefore, a possible measurement can be done by comparing the spectra at V1 (grounded) and at the “out” line, after both the RC filter and the SPST. The “test line” shown in figure 22 has to be removed, otherwise the same noise filtered by the RC circuit will be re-introduced. The “control line” has been connected to V+, to keep the SPST in the closed state.

Power spectra are taken with the fast-Fourier transform option of the oscilloscope. Figure 24 shows the presence of noise at the input V1 (black lines), originated from the power supply or picked up from the lines, that gets significantly filtered in the CEB to a level of ≈ -105 dB (red lines). There are no visible differences between measurements at 300 K (left), and 4 K (right).

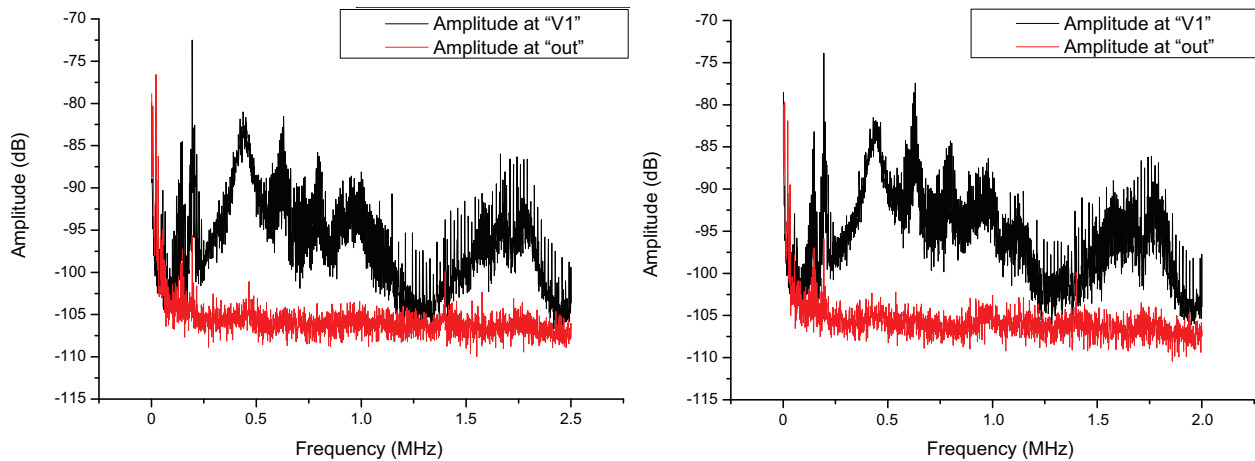


Figure 24: Noise spectra at 300 K (left), and 4 K (right).

Crosstalk Crosstalk is defined as the introduction of noise at the (analog) output of the SPST coming from the digital side, and is mainly due to parasitic capacitive couplings between the two.

To quantify the frequency-dependent coupling between control line and output of the SPST, the setup shown in figure 22 has been used. The “test line” has been removed, V1 connected to ground, and the “control line” connected to both the spectrum analyser and a signal generator. This latter supplies a 50 kHz square wave (50% duty cycle, 2 V amplitude), which has the spectrum shown by the black line in figure 25. Many peaks are present, since a square wave of frequency f can be thought as the infinite sum of sine waves with frequencies $(2n+1)f$ (n -integer), and therefore its Fourier transform (spectrum) is an infinite sum of Dirac’s delta functions. By measuring the spectrum at the “out” line, it is possible to quantify how much each one of these peaks gets coupled to the output, and therefore also to understand how the crosstalk with the control line depends on the frequency.

Two different crosstalk measurements have been taken, respectively with the SPST in the closed and open states. This has been done by changing the offset of the square wave, in such a way that even if the control

signal fluctuates, the SPST state does not change ($V_{\text{offset}} \approx \pm 5 \text{ V}$). From figure 25 it is possible to see that the crosstalk is independent on the state of the SPST, since the spectra taken for the two different cases overlap, and almost the same at 300 K (left) and 4 K (right). Crosstalk can be seen for frequencies lower than 500 kHz, with an attenuation > 50 dB, and approximately between 1.1 MHz and 1.4 MHz, with an attenuation > 60 dB.

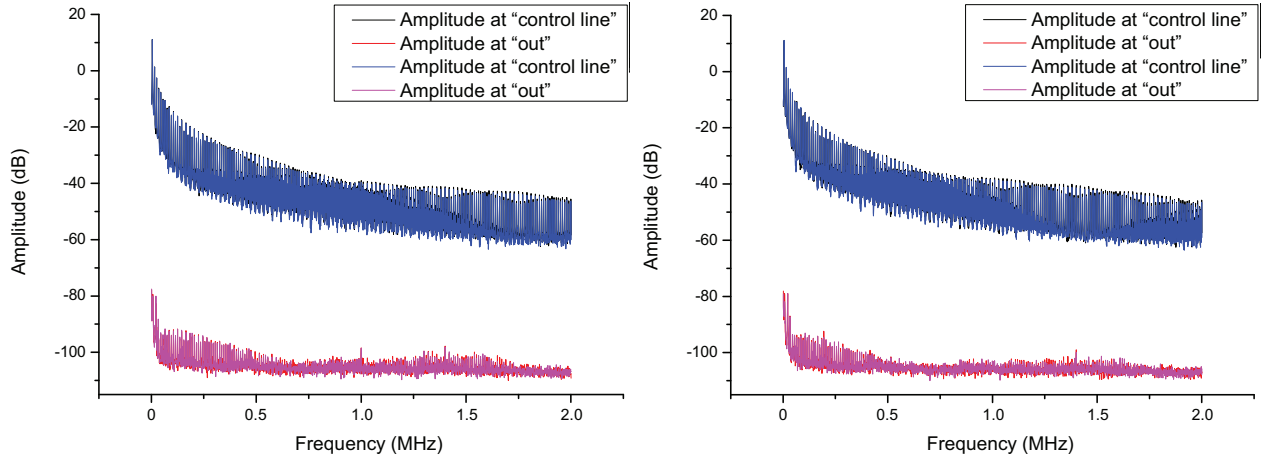


Figure 25: Crosstalk spectra at 300 K (left), and 4 K (right), for the SPST open (black-red) and closed (blue-violet). Curves for the open and closed cases overlap, shaded features in the plots are due to the finite sampling rate of the spectrum analyser.

Open impedance When the SPST is open it acts like a capacitor with a finite impedance for AC signals. To measure the frequency-dependent impedance presented by the SPST in the open state, the setup shown in figure 22 has been used. For the same reason as in the crosstalk measurement, a 50 kHz square wave (50% duty cycle, 2 V amplitude) has been applied to V1, while the “control line” has been connected to V₋, to keep the SPST in the open state.

Spectra have been measured at V1 and at the “out” line (figure 26). Measurements show a variation in the switch off-impedance between 300 K (left) and 4 K (right). At 4 K it is possible to observe transmission of signals with frequencies lower than 500 kHz, with an attenuation > 50 dB, and approximately between 1.2 MHz and 1.4 MHz, with an attenuation > 60 dB.

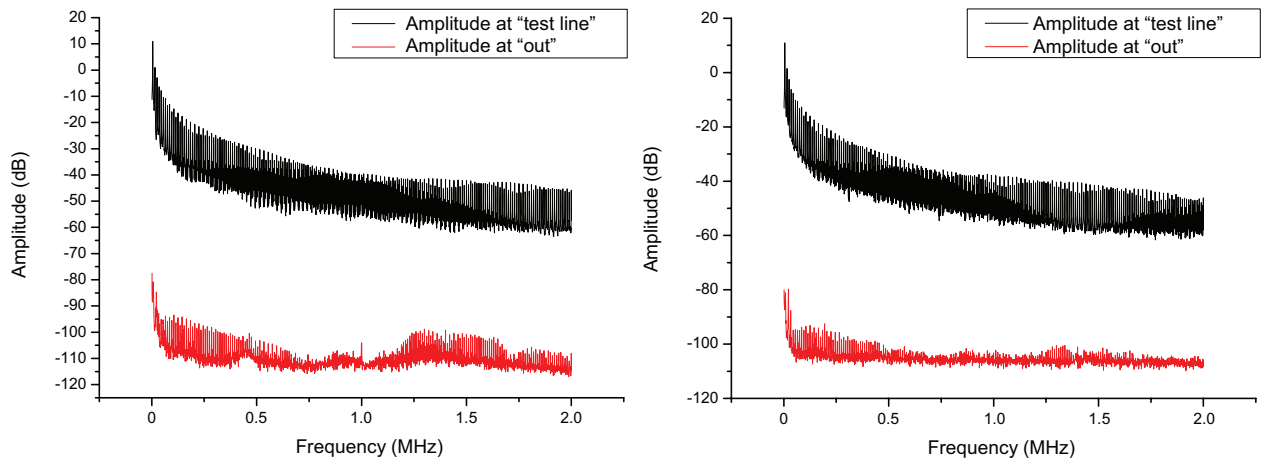


Figure 26: Impedance spectra at 300 K (left), and 4 K (right). Shaded features in the plots are due to the finite sampling rate of the spectrum analyser.

FET Cryo Buffer setup To perform precise time-dependent measurements (rise/fall times, jitter), the setup shown in figure 27 has been used, where a cryo-compatible buffer has been added between two SPSTs outputs and the coaxial cable (to match the high impedance of the SPSTs outputs to the 50Ω impedance of the cable).

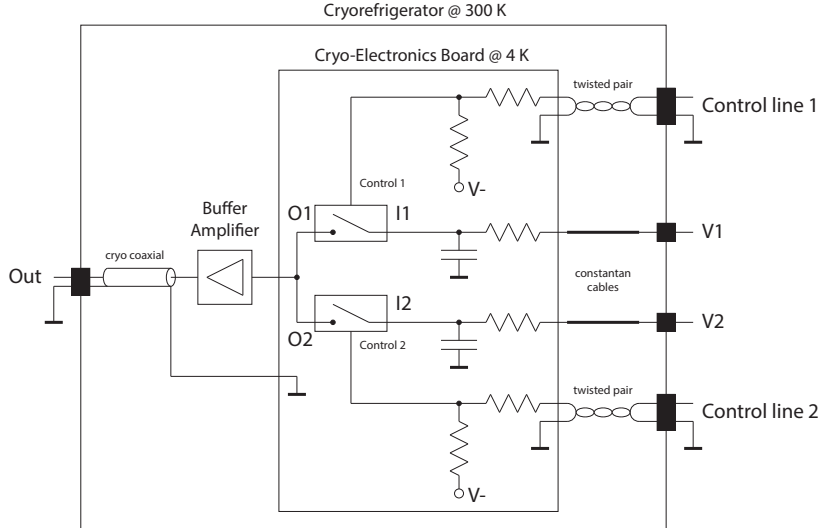


Figure 27: Measurement setup for rising/falling times and jitter.

The active device of the buffer is a GaAs FET NE3510, manufactured by NEC [41]. High cutoff frequency (2 GHz) and cryo-compatibility make it suitable for the application [42]. Figure 28 shows the schematic of the buffer amplifier.

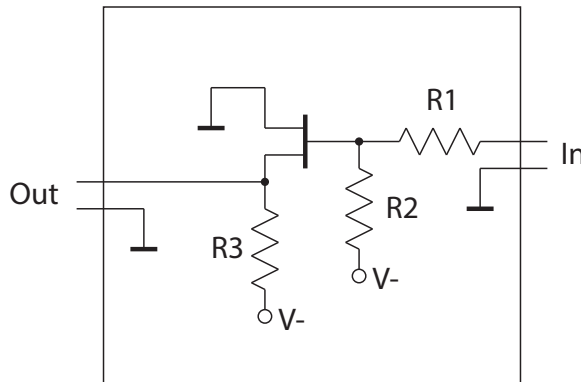


Figure 28: Schematic of the cryo-FET buffer.

The components have the following functions:

- $R1 = 4.7\text{ k}\Omega$, $R2 = 1\text{ k}\Omega$ form a voltage divider to attenuate the output signal from the switch, which spans over 9 V, to $< 2\text{ V}$ (maximum gate voltage allowed by the FET). They also ensure the correct biasing of the FET, in order to have unitary gain,
- $R3 = 50\Omega$ is the resistor which determines the output impedance of the buffer (which has to match the one of the coaxial cable).

Both “control lines” in figure 27 have been driven by pulses obtained by the digital control setup shown in figure 21 (which involves the low-jitter pulse generator BNC745). A variable power supply has been connected to V1 and V2, allowing to perform measurements for different voltage steps.

Due to FET limitations, measurements at 4 K have been done only for output signals with amplitude $< 2 \text{ V}$. Only at 300 K, with the cryorefrigerator open, measurements at the full scale needed for the experiments ($\approx 10 \text{ V}$) have been done by connecting the oscilloscope directly at the switch output (O1+O2) with a short ($\approx 50 \text{ cm}$) coaxial cable.

Figure 29 shows the amplified pulse seen from the scope at the “out” line. ΔV_1 and ΔV_2 are the voltage steps with respect to a reference voltage. Ripples are due to ringing in the coaxial cable (their duration depends in its length, increasing by $\approx 100 \text{ ns}$ per meter of cable, as expected given the speed of light in the conductor), and therefore they are not expected to be present at the trap electrodes when the cable will be removed. The last slow falling edge in figure 29 corresponds to the discharging of the capacitance shown by the coaxial cable, through the resistor $R_3=50 \Omega$ of the buffer.

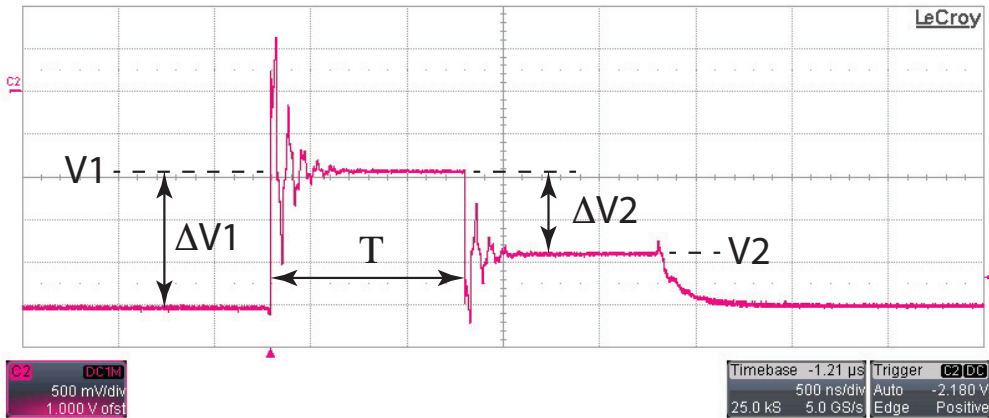


Figure 29: Pulse seen from the oscilloscope, connected with a 2 m long coaxial cable to the FET-buffer at 4 K.

Rise/fall times As explained at the beginning of this section, one of the main requirements to perform the experiments proposed is the ability to switch between different potentials in nanosecond timescales. The setup used for the measurement is the one shown in figure 27. Rise/fall times have been measured as the time elapsed between 10% and 90% of the amplitude of an edge.

Measurements for a pulse like the one in figure 29 have been taken for different voltage steps ΔV_1 (figure 30 (left)) and ΔV_2 (figure 30 (right)). For a voltage step $\Delta V_1 < 2 \text{ V}$, measurements with the buffer show rise/fall times $\approx 30\%$ lower at 4 K than at 300 K, and increasing with the step amplitude. Measurements without the buffer at 300 K show almost constant rise/fall times for voltage steps $\Delta V_1 < 2 \text{ V}$, as expected from the datasheet of the switches, which quotes rise/fall times independent of the voltages switched [37]. These measurements suggest that the voltage-dependent switching time seen with the FET plus the long coaxial cable could be due to the load posed by them.

Jitter Another important requirement discussed before is a low jitter in the time-dependent (periodic) voltages going to the electrodes ($< 20 \text{ ps}$ is desirable). Here, the jitter δt is defined as the standard deviation of the distribution of periods taken over many periods ($\approx 30 \text{ s}$) (figure 31). For a trapped ion, the jitter in

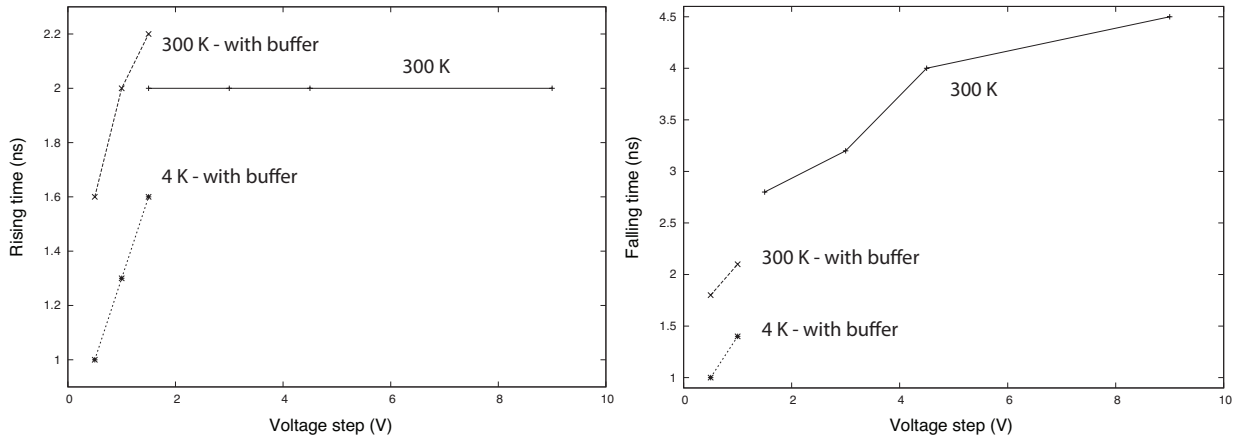


Figure 30: Rise (left) and fall (right) times, at 300 K and 4 K, with and without the FET-buffer. Measurements labelled “300 K” are taken with the cryorefrigerator open, by connecting the scope directly to the CEB with a short cable.

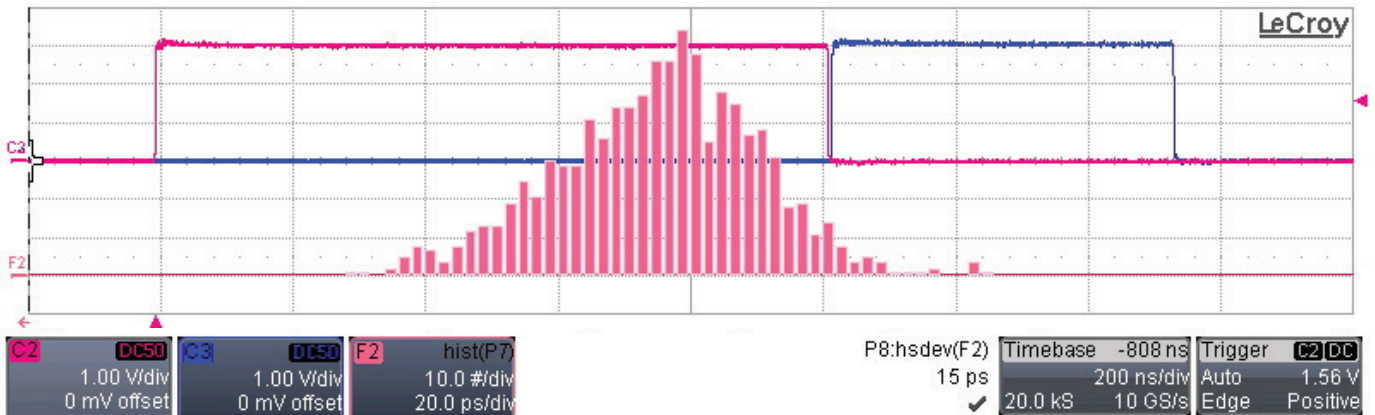


Figure 31: Distribution (histogram) of the periods between the rising edges of the red and blue pulses. The jitter corresponds to the standard deviation of the distribution, which is 15 ps in this case.

the electrode potential shown in figure 20 corresponds to different durations of the transport potential well and different “catching” times, that might cause the trapping of a state with non-zero mean momentum.

Measurements for a pulse like the one in figure 29 have been taken as the jitter in the time T^1 , in two cases. The first case is for fixed width $T = 500$ ns and different voltage steps ΔV_2 , keeping ΔV_1 at 1.5 V when the buffer is connected and at 9 V otherwise (figure 32 (left)). The second case is for constant voltage steps $\Delta V_1 = 1$ V, $\Delta V_2 = 0.5$ V, and different widths T (figure 32 (right)). Measurements show a jitter decreasing with the voltage step and with the temperature (as expected since thermal noise introduces jitter) and a jitter increasing with the pulse width, that is originated from the clock and the delay circuitry inside the pulse generator.

Sources of jitter The main sources of jitter are the time accuracy of the clock used to generate the periodic signal, and noise. Electronics and long cables can introduce noise in the signal and therefore increase the jitter.

¹Note that the jitter in the width T of the pulse in figure 29 is directly related to the jitter between two edges of the digital control signal generating the pulse itself (figure 20).

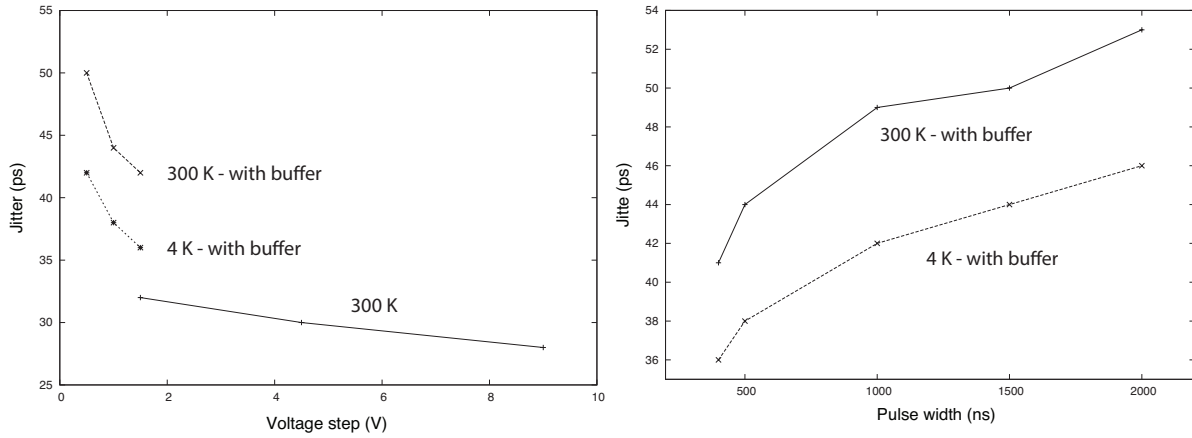


Figure 32: Jitter, at 300 K and 4 K, with and without the FET-buffer. Measurements labelled “300 K” are taken with the cryorefrigerator open, by connecting the scope directly to the CEB with a short cable.

Using the setup shown in figure 21 it is possible to see that the jitter in the period between two pulses (of 500 ns width, as in figure 31) is ≈ 15 ps at the output of the pulse generator, and ≈ 35 ps after the amplification electronics. Note that this jitter was measured using two different channels of the oscilloscope, while the jitter of ≈ 30 ps at the switch output was measured using only one channel (which keeps the contribution for the jitter of the scope to a minimum).

Figure 33 shows the fluctuations in the period between two pulses (of 500 ns width, as in figure 31) at the output of the pulse generator, for different timescales. From the Fourier transform of this data (figure 34), it is possible to see that fluctuations in all timescales are randomly distributed around a horizontal line (as would be expected from jitter), showing that no periodicity or drift is present.

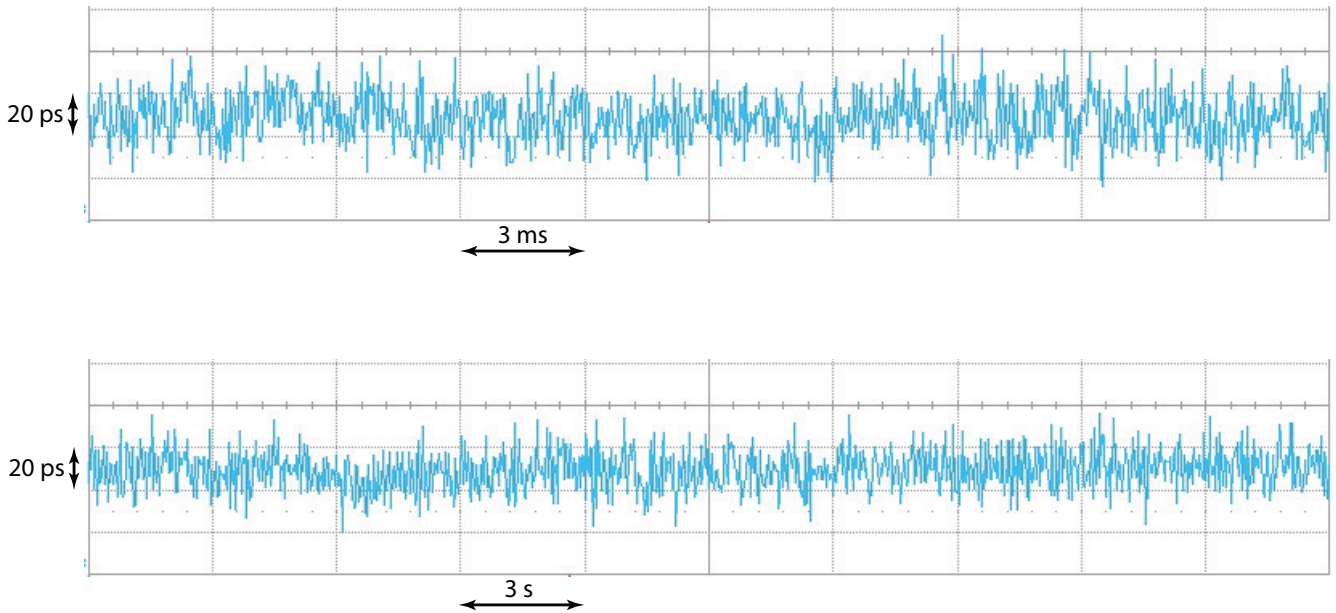


Figure 33: Periods between two pulses taken over two different timescales.

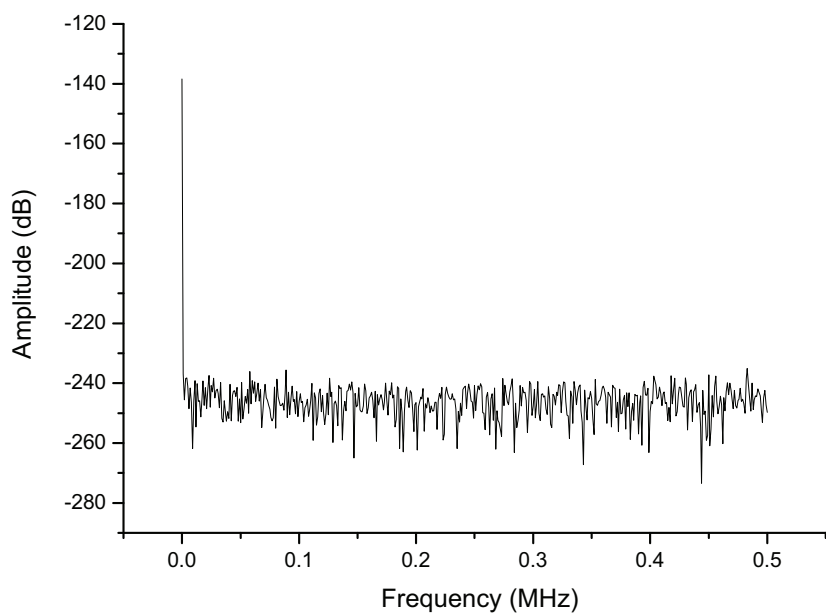


Figure 34: Fourier transform of the periods between two pulses.

6 Summary

In this thesis, the experimental setup needed to control the quantum motional state of a trapped ion faster than its oscillation period has been presented. For the cryo-electronics developed, the main requirements are satisfied and performances are promising (table 6).

	300 K	4 K
Off resistance	$> 10 \text{ M}\Omega$	$> 10 \text{ M}\Omega$
On resistance	12Ω	3.5Ω
Power cons. switching at 1 MHz	8 mW	10 mW
Vout/Vin (Linearity)	/	0.9888
Noise	-105 dB	-105 dB
Crosstalk at 1.5 MHz	-100 dB	-100 dB
Off impedance at 1.5 MHz	-100 dB	-100 dB
Rising time for 1 V	2 ns	1.3 ns
Falling time for 1 V	2.1 ns	1.4 ns
Jitter	42 ps	36 ps

Table 6: Summary of the performance of the switching electronics at 300 K and 4 K.

A definitive solution for the generation of the digital control signals needed to drive the switches has not yet been found, so a number of different devices will be tested in the next months.

The setup proposed will be used to perform new experiments, aimed to test possibilities for speeding up the transport of ions in segmented ion traps, to prepare non-classical states of the motion, and also to control multiple ions in a string faster than the Coulomb interaction between them. Fast control of the trapping potential could also be used for other applications, such as the realization of schemes which have been proposed for entanglement generation and the investigation of continuous-variable quantum information processing [43, 44].

Future projects might include the test of other electronic devices at 4 K, like microcontrollers and DACs. In principle, among other possibilities, they would allow to apply arbitrary potentials at the trap electrodes, at timescales at least as fast as the switches used in this work. In this regard, the digital signal processor dsPIC30F6010 from Microchip has been tested to work at 4 K, with a clock frequency of 5 MHz.

References

- [1] H.G. Dehmelt, *Adv. At. Mol. Phys.* **3**, (1967) 53
- [2] P.K. Ghosh, *Ion traps* (Clarendon, Oxford, 1996)
- [3] F.G. Major, V.N. Gheorghe, G. Werth, *Charged particle traps* (Springer, Berlin, 2005)
- [4] J.I. Cirac, P. Zoller, *Phys. Rev. Lett.* **74** (1994) 4091
- [5] J.D. Jost, J.P. Home, J. M. Amini, D. Hanneke, R. Ozeri, C. Langer, J.J. Bollinger, D. Leibfried, D.J. Wineland, *Nature (London)* **459** (2009) 683

References

- [6] K.R. Brown, C. Ospelkaus, Y. Colombe, A.C. Wilson, D. Leibfried, D.J. Wineland, *Nature* **471**, (2011) 196
- [7] D.M. Meekhof, C. Monroe, B.E. King, W.M. Itano, D.J. Wineland, *Phys. Rev. Lett.* **76** (1996) 1796
- [8] C. Monroe, D.M. Meekhof, B.E. King, D.J. Wineland, *Science* **272** (1996) 1131
- [9] C.J. Myatt, B.E. King, Q.A. Turchette, C.A. Sackett, D. Kielpinski, W.M. Itano, C. Monroe, D.J. Wineland, *Nature* **403**, (2000) 269
- [10] M.J. McDonnell, J.P. Home, D.M. Lucas, G. Imreh, B.C. Keitch, D.J. Szwer, N.R. Thomas, S.C. Webster, D.N. Stacey, A.M. Steane, *Phys. Rev. Lett.* **98** (2007) 063603
- [11] P.C. Haljan, K.-A. Brickman, L. Deslauriers, P.J. Lee, C. Monroe, *Phys. Rev. Lett.* **94** (2005) 153602
- [12] F. Zähringer, G. Kirchmair, R. Gerritsma, E. Solano, R. Blatt, C.F. Roos, *Phys. Rev. Lett.* **104** (2010) 100503
- [13] R. Bowler, J. Gaebler, Y. Lin, T.R. Tan, D. Hanneke, J.D. Jost, J.P. Home, D. Leibfried, D.J. Wineland, arXiv:1206.0780 (2012)
- [14] A. Walther, F. Ziesel, T. Ruster, S.T. Dawkins, K. Ott, M. Hettrich, K. Singer, F. Schmidt-Kaler, U. Poschinger, arXiv:1206.0364 (2012)
- [15] M.A. Rowe, A. Ben-Kish, B. DeMarco, D. Leibfried, V. Meyer, J. Beall, J. Britton, J. Hughes, W.M. Itano, B. Jelenkovic, C. Langer, T. Rosenband, and D.J. Wineland, *Quantum Information and Computation* **2**, (2002) 257-271
- [16] W.K. Hensinger, S. Olmschenk, D. Stick, D. Hucul, M. Yeo, M. Acton, L. Deslauriers, C. Monroe, J. Rabchuk, *Appl. Phys. Lett.* **88** (2006) 034101
- [17] J.M. Amini, H. Uys, J.H. Wesenberg, S. Seidelin, J. Britton, J.J. Bollinger, D. Leibfried, C. Ospelkaus, A.P. VanDevender, D.J. Wineland, *New J. Phys.* **12** (2010) 033031
- [18] D.L. Moehring, C. Highstrete, M.G. Blain, K. Fortier, R. Halti, D. Stick, C. Tigges, *New J. Phys.* **13** (2011) 075018
- [19] R.B. Blakestad, C. Ospelkaus, A.P. VanDevender, J.M. Amini, J. Britton, D. Leibfried, D.J. Wineland, *Phys. Rev. Lett.* **102** (2009) 153002
- [20] J. Alonso, F.M. Leupold, B.C. Keitch, J.P. Home, *New J. Phys.* **15** (2013) 023001
- [21] J. Chiaverini, R.B. Blakestad, J. Britton, J.D. Jost, C. Langer, D. Leibfried, R. Ozeri, D.J. Wineland, *Quantum Inf. Comput.* **5** (2005) 419
- [22] D.J. Wineland, C. Monroe, W.M. Itano, D. Leibfried, B.E. King, D.M. Meekhof, *J. Res. Natl. Inst. Stand. Technol.* **103**, (1998) 259
- [23] R.W. Henry and S.C. Glotzer, *Amer. J. Phys.* **56** (1988) 318-328
- [24] A. Serafini, A. Retzker, M.B. Plenio, *New J. Phys.* **11** (2009) 023007

References

- [25] W. E. Gifford and R. C. Longsworth, Adv. Cryogen. Eng. **10B**, (1965) 69
- [26] R. Radebaugh, J. Zimmerman, D. R. Smith, B. Louie, Adv. Cryogen. Eng. **31**, (1986) 779
- [27] E. I. Mikulin, A. A. Tarasov, M. P. Shkrebyonock, Adv. Cryogen. Eng. **29**, (1984) 629
- [28] R. Radebaugh, Proc. Inst. Refrig. **96**, (2001) 11
- [29] W. Rawlins, R. Radebaugh, P. E. Bradley, K. D. Timmerhaus, Adv. Cryogen. Eng. **39**, (1994) 1449
- [30] S. Zhu, P. Wu, Z. Chen, Cryogen. **30**, (1990) 514
- [31] Y. Matsubara and J. L. Gao, Cryogen. **34**, (1994) 259
- [32] CRYOMECH, PT410 specification sheet
- [33] C. Wang, Cryocoolers **15**, (1994) 177
- [34] W.W. Macalpine, R.O. Schildknecht, Proc. IRE **47**, (1959) 2099
- [35] S. Ulmer, Diploma thesis (Mainz, 2006)
- [36] R. Hablutzel, Diploma thesis (Zürich, 2012)
- [37] Texas Instruments, datasheet from CD54HC4066, CD74HC4066, CD74HCT4066 High-Speed CMOS Logic Quad Bilateral Switch
- [38] Picosecond, datasheet from model 12000 pulse/pattern generator
- [39] Highland Technology, datasheet from model P400 pulse generator
- [40] Berkeley Nucleonics, datasheet from Model 745 250 fs Digital Delay Generator
- [41] NEC, datasheet from NE3510 GaAs FET
- [42] S. Stahl, private communication
- [43] J.P. Home, M.J. McDonnell, D.J. Szwer, B.C. Keitch, D.M. Lucas, D.N. Stacey, A.M. Steane, Phys. Rev. A **79** (2009) 050305(R)
- [44] D. Hanneke, J.P. Home, J.D. Jost, J. Amini, D. Leibfried, D.J. Wineland, Nature Physics **6** (2010) 13